Table 3-2 Initial Hydraulic Conductivity Values for the Groundwater Flow Model

Hydrostratigraphic Unit	Horizontal Hydraulic Conductivity (ft/day)	Vertical Hydraulic Conductivity (ft/day)
"A" horizon	1.3	$2.84x10^{-3}$
"AA" horizon	9.5	$2.06x10^{-2}$
transmissive zone (TZ)	25.4	0.292
tan clay confining zone (TCCZ)	0.5	$2.5x10^{-3}$
middle aquifer zone (MAZ)	10.0	0.25
tan clay lower clay (TCLC)	2.2	$2.0x10^{-3}$
lower aquifer zone (LAZ)	27.9	$1.0x10^{-2}$

3.4 Assumptions

The use of simplifying assumptions is inherent in all model developments. For the RRSB groundwater flow model, assumptions were made to define the location and magnitude of the boundary conditions and to assign model parameters.

The use of constant-head boundary conditions was necessary given the requirement of developing a localized model for the RRSB and the lack of natural local flow boundaries for the deeper hydrostratigraphic layers. The magnitude of the constant-head boundaries was extrapolated from the known head measurements for each layer. However, given the limited number of data points in some of the units, it is assumed that the extrapolation of these heads to the location of the boundaries has little impact on the overall solution near the RRSB.

The model was developed with the intention of using single horizontal and vertical hydraulic conductivity values per unit. This assumption disregards the impact of any heterogeneity present within the individual hydrostratigraphic units. However, to obtain a good calibration to the observed heads, only a slight modification to the conductivity fields in the upper soil horizons was required.

Given that a steady-state solution to the groundwater flow field would be developed, it was assumed that the average water levels would best approximate the expected flow paths.

3.5 Discretization of the Model Domain

A plan view of the active grid developed for the numerical model is presented in Figure 3-8. The active region of the grid consists of 105 rows by 102 columns. The grid cell dimensions are 25 ft by 25 ft in the vicinity of the seepage basins. As shown in Figure 3-1, the model is discretized into 20 vertical layers (Table 3-3). Figure 3-9 presents an oblique view of a set of cross sections through the model grid along the cross-sectional lines shown in Figure 3-8. These cross sections show the variable thickness of the units across the model domain. Notice the variability in the

thickness of the TCCZ and MAZ layers. Also, notice that the thickness of the upper "undifferentiated" surface soils/"A" horizon unit, hereafter known as the "A" horizon, decreases towards Mill Creek to the north and west (B-B' and C-C') and towards Joyce Branch to the east (A-A').

Table 3-3 Vertical Layers in the Saturated-Zone Flow and Transport Models

Model Layers	Hydrostratigraphic Unit
1 - 2	"A" horizon
3 - 6	"AA" horizon
7 - 10	transmissive zone (TZ)
11 – 12	tan clay confining zone (TCCZ)
13 – 14	middle aquifer zone (MAZ)
15 – 16	tan clay lower clay (TCLC)
17 – 20	lower aquifer zone (LAZ)

3.6 Flow Model Calibration Results

For the saturated-zone flow model, the vertical and horizontal hydraulic conductivity values for each of the hydrostratigraphic units were varied until a set of values was obtained that best reproduced the average potentiometric surfaces for each unit. The water-table potentiometric surface for the calibrated steady-state groundwater flow model, which intersects both the "A" and "AA" soil horizons, is presented in Figure 3-10. The potentiometric surfaces for the TZ, MAZ, and the LAZ are presented in Figures 3-11 through 3-13. The observed and the computed head values for the observation wells used in the calibration process were compared and the residuals are presented in Table 3-1. The error statistics for the calibrated flow model, which are based on these observation wells, include a mean error in the heads of -0.29 ft, a mean absolute error of 2.39 ft and a root mean square (RMS) residual of 2.99 ft. Figure 3-14 presents plots of the observed head versus computed head and the observed head versus residual for each of the observation monitoring wells. The observation well symbols are color coded to the hydrostratigraphic units. This figure shows that the maximum spread in the errors is +/- 7 ft, with the majority of this spread resulting from the observation wells located in the upper two soil horizons (the "A" and the "AA").

Table 3-4 presents the calibrated hydraulic conductivity values for each hydrostratigraphic unit. From a review of the observed range in hydraulic conductivity values across the SRS and at the R-Reactor Area (WSRC, 2000a; WSRC, 2000b; WSRC 2001a), the calibrated values obtained for each of the seven hydrostratigraphic units are consistent with the observed data. Multiple hydraulic conductivity zones were necessary in all units, except the TCLC and LAZ, to maintain the heads within and just to the south of the basin area. The distributions of the hydraulic conductivity zones required to obtain a satisfactory fit to the observed heads are presented in Figures 3-15 and 3-16. Figure 3-15 shows the location of the hydraulic conductivity zones for both the "A" and the "AA" horizons. The yellow lines on the figure denote the hydraulic-

conductivity zone boundaries and the shading shows the elevation of the lower contact for the respective hydrostratigraphic unit. For each of the units within the model, a low area or depression is located just to the south of the seepage basins and runs north-northeast through the basin area. This area of structural depression is observed for the "A" and "AA" soil horizons in Figure 3-15. This depression may be composed of a higher percentage of finer grain sediments which would result in a region of lower vertical hydraulic conductivity values, as required during the model calibration process. Figure 3-16 presents the hydraulic conductivity zones for the TZ, TCCZ and the MAZ.

Given the relatively low hydraulic conductivity of the upper two units and the predominantly vertical flow within the units, as discussed below, the impact of these zones on the future transport flow paths was not significant. For both the "A" and "AA" horizon, the hydraulic conductivity within the drain cells that define the location of Mill Creek, the R-Effluent Discharge Canal, Pond A and Joyce Branch was increased in the vertical direction to allow for upward flow and subsequent discharge.

Table 3-4 Calibrated Hydraulic Conductivity Values

Hydrostratigraphic Unit	Zone	Hydraulic Conductivity (ft/day)	
		Horizontal	Vertical
"A" horizon	1	0.41	0.41
	2	0.41	5.0×10^{-2}
	3	0.41	5.0×10^{-3}
	4	0.41	4.0×10^{-2}
"AA" horizon	1	0.75	0.38
	2	0.75	3.0×10^{-2}
	3	0.38	1.0×10^{-2}
TZ	1	8	9.8×10^{-2}
	2	8	6.0×10^{-2}
TCCZ	1	15	7.2×10^{-3}
	2	4	1.5×10^{-4}
	3	8.4×10^{-2}	9.8×10^{-2}
MAZ	1	20	0.72
	2	20	1.5×10^{-4}
TCLC		4	1.5×10^{-4}
LAZ		30	9.0×10^{-2}

3.7 Particle Track Analysis

Particle tracking simulations were conducted using MODPATH (Pollack, 1994). These results demonstrate that, based on the large vertical head gradients between the hydrostratigrahic units, the flow of groundwater in the vicinity of the RRSB is predominantly vertical from the "A" horizon down through the TZ and TCCZ. Significant lateral flow is not observed until the particles travel through the TCCZ and enter the lower permeable units.

In particle tracking simulations, particle flow line calculations are based solely on advective transport with no retardation, decay, or dispersion incorporated. The results of the particle-tracking simulations are presented in Figures 3-17 through 3-19. Figure 3-17 shows the lateral pathways of several particles dropped at the surface of the water table beneath the seepage basins, along the sanitary sewer line to the west of the basins, and in an area of known contamination located to the south and east of the existing asphalt cover. A string of particles was released from each basin to evaluate the pathways basin by basin (Figure 3-18). Except for Basins 3 and 4, the pathlines from each basin are in the same direction. At Basin 3, particles released at the southern end of the basin generally travel to the southeast and particles released at the northern end of the basin trend to the north. The particle released at the northernmost end of Basin 4 initially trends to the north, but then changes direction and travels to the east. The particle tracks in Figures 3-17 and 3-18 show that there is lateral advective-only flow away from the seepage basins, but to determine which units the particles migrate through, cross sections were created along pathways of selected particles released from the six seepage basins (Figure 3-19). The cross sections of the particle pathlines indicate that the transport away from the RRSB is predominantly vertical through the "A" and "AA" horizons, vertical with a horizontal component through the TZ, vertical through the TCCZ and then predominantly horizontal through the MAZ, TCLC and LAZ. As depth increases, the impact of the surface topography and the shallow flow fields on flow direction decreases and the impacts of the more regional scale flow patterns emerge.

The surface-water bodies within the model domain include Mill Creek, the R-Effluent Canal, Pond A and Joyce Branch (see Figure 3-17). Based on the particle track results, the groundwater that infiltrates through the RRSB OU source region and into the saturated zone does not discharge directly to any of these surface-water bodies.

3.8 Sensitivity Analysis

To gain a better understanding of the important influences on the groundwater flow in R-Area, a detailed sensitivity analysis was performed. The analysis was done for several cases; in each case, a single input parameter of the basecase flow model was varied while all other inputs were held constant. Parameters that were varied during the simulations included global recharge, selected vertical hydraulic conductivities, and selected horizontal hydraulic conductivities (see Table 3-5). Changes in the model output for each case were evaluated by recording the error in the computed and observed heads, flow between hydrostratigraphic layers, and baseflows for the streams and the canal. A complete listing of these results is shown in Table 3-6. Sensitivity simulations that did not converge are identified as DNC in Table 3-6. Labels for the curves shown in Figures 3-20 through 3-29 are also identified in Table 3-6.

Figure 3-20 shows the variation in root mean squared (RMS) error with each parameter. The most sensitive parameters, as reflected by the RMS, were global recharge, horizontal hydraulic conductivity in the MAZ, and vertical hydraulic conductivity in the "AA". Figures 3-21 and 3-22 indicate that downward flow from the "A" and the "AA" horizons is most sensitive to the global recharge rate. Downward flow from the TZ and TCCZ is most sensitive to the vertical hydraulic conductivity of the TCCZ as well as to changes in the horizontal hydraulic

conductivity of the MAZ (Figures 3-23 and 3-24). Downward flow from the MAZ and TCLC is most sensitive to the vertical hydraulic conductivity of the TCLC (Figures 3-25 and 3-26). The majority of the computed baseflows from Joyce Branch and Mill Creek come from the TZ, while only a small amount discharges from the "A" and "AA" horizons. As a result, baseflows from Joyce Branch and Mill Creek are most sensitive to changes in the horizontal hydraulic conductivity of the TZ (Figures 3-27 and 3-28). Figure 3-29 shows that computed baseflows to the R-Effluent Canal and Pond A are most sensitive to changes in the global recharge.

Table 3-5 Parameter Values Used in the Flow Model Sensitivity Analysis

Parameter	Description	Calibrated Value	Sensitivity Range	
			Minimum	Maximum
Recharge (in/yr)	Global	15	5	25
Vertical Hydraulic Conductivity (ft/day)	"A" horizon, Zone 3 (Kv_a3)	5.0×10^{-3}	5.0×10^{-4}	5.0×10^{-2}
	"AA" horizon, Zone 3 (Kv_aa3)	1.0×10^{-2}	5.0×10^{-4}	5.0×10^{-2}
	TZ, Zone 1 (Kv_tz1)	9.8×10^{-2}	9.8×10^{-3}	0.98
	TCCZ, Zone 1 (Kv_tccz1)	7.0×10^{-3}	7.0×10^{-4}	7.0×10^{-2}
	MAZ, Zone 1 (Kv_maz1)	0.72	7.2×10^{-2}	7.2
	TCLC (Kv_tclc)	1.5×10^{-4}	1.5E-05	7.7×10^{-3}
	LAZ (Kv_laz)	9.0×10^{-2}	9.0×10^{-3}	0.9
Horizontal Hydraulic Conductivity (ft/day)	"A" horizon, All Zones (Kh_a)	0.41	4.1×10^{-2}	4.1
	"AA" horizon, Zone 3 (Kh_aa3)	0.38	3.8×10^{-2}	19
	TZ, All Zones (Kh_tz)	8	0.8	80
	MAZ, All Zones (Kh_maz)	20	2	200
	LAZ (Kh_laz)	30	3	300

Table 3-6 Flow Model Sensitivity Analysis Results

Parameter	Value	Factor of Basecase Values	Mean Error	Abs Mean Error	RMS	Flow (ft^3/day) from lower face of layer bottom in hydrostratigraphic unit.						Baseflows (ft^3/day)		
						"A horizon"	"AA horizon"	TZ	TCCZ	MAZ	TCLC	Joyce Branch	R-Effluent Canal	Mill Creek
Recharge	5	0.33	-6.38	6.54	7.89	18218	17590	34925	34870	7263	2181	32344	12752	14713
Recharge	10	0.67	-3.33	3.76	4.86	36033	34247	40987	40930	7842	2408	32892	13206	16309
Recharge	15	1.00	-0.29	2.39	2.99	53259	50462	46745	46687	8397	2628	32613	13868	18196
Recharge	20	1.33	5.67	5.90	7.12	70702	66579	52265	52206	8936	2842	34398	15292	20354
Recharge	25	1.67	DNC	DNC	DNC	DNC	DNC	DNC	DNC	DNC	DNC	DNC	DNC	DNC
Kv_a3	$5.0x10^{-4}$	0.1	0.77	2.72	3.39	53257	50460	46716	46658	8389	2624	33637	13868	18197
Kv_a3	$2.5x10^{-3}$	0.5	0.13	2.40	2.99	53258	50461	46733	46676	8394	2626	33640	13868	18496
Kv_a3	$5.0x10^{-3}$	1	-0.29	2.39	2.99	53259	50462	46745	46687	8397	2628	32613	13868	18196
Kv_a3	$7.5x10^{-3}$	1.5	-0.53	2.44	3.08	53259	50462	46751	46694	8398	2629	33640	13868	18196
Kv_a3	$5.0x10^{-2}$	10	-1.28	2.80	3.55	53261	50463	46773	46715	8404	2631	33638	13868	18194
Kv_aa3	$5.0x10^{-4}$	0.05	2.12	3.48	5.16	53257	50460	46716	46658	8389	2625	33712	13884	18216
Kv_aa3	$2.5x10^{-3}$	0.25	1.07	2.77	3.79	53191	50415	46849	46791	8404	2631			
Kv_aa3	$7.5x10^{-3}$	0.75	0.02	2.40	3.00	53244	50473	46762	46704	8398	2629			
Kv_aa3	$1.0x10^{-2}$	1	-0.29	2.39	2.99	53259	50462	46745	46687	8397	2629	32613	13868	18196
Kv_aa3	$5.0x10^{-2}$	5	-1.26	2.80	3.55	53318	50552	46652	46594	8389	2625	33705	13860	18184
Kv_tzl	$9.8x10^{-3}$	0.1	DNC	DNC	DNC	DNC	DNC	DNC	DNC	DNC	DNC	DNC	DNC	DNC
Kv_tzl	$4.9x10^{-2}$	0.5	DNC	DNC	DNC	DNC	DNC	DNC	DNC	DNC	DNC	DNC	DNC	DNC
Kv_tzl	$9.8x10^{-2}$	1	-0.29	2.39	2.99	53259	50462	46745	46687	8397	2628	32613	13868	18196
Kv_tzl	0.15	1.5	0.15	2.47	3.17	53275	50985	49361	49303	8468	2652			
Kv_tzl	0.98	10	-0.13	2.55	3.21	53404	54004	52695	52636	8542	2676	36875	13987	21126
Kv_tccz1	$7.0x10^{-4}$	0.1	DNC	DNC	DNC	DNC	DNC	DNC	DNC	DNC	DNC	DNC	DNC	DNC
Kv_tccz1	$3.6x10^{-3}$	0.5	0.35	2.40	2.98	53048	50015	32220	32165	8160	2153	33464	14126	18138
Kv_tccz1	$7.1x10^{-3}$	1	-0.29	2.39	2.99	53259	50462	46745	46687	8397	2628	32613	13868	18196
Kv_tccz1	$1.1x10^{-2}$	1.5	-0.54	2.39	3.02	53329	50628	47960	47901	8626	2694			
Kv_tccz1	$7.0x10^{-2}$	9.8	-1.17	2.56	3.24	53508	50987	91487	91431	8917	2777	37022	13535	23580
Kv_maz1	$7.2x10^{-2}$	0.1	-0.20	2.38	2.97	53239	50415	44742	44683	8300	2587	33640	13907	18136
Kv_maz1	0.36	0.5	0.24	2.39	2.98	53257	50457	46482	46424	8385	2623	33639	13873	18189
Kv_maz1	0.72	1	-0.29	2.39	2.99	53259	50462	46745	46687	8397	2628	33640	13868	18196
Kv_maz1	3.6	5	0.22	2.39	2.99	53261	50467	46968	46911	8406	2632	33639	13865	18203
Kv_maz1	7.2	10	0.22	2.39	2.99	53261	50467	46997	46940	8407	2632	33639	13865	18204
Kv_tclc	$1.5x10^{-5}$	0.1	DNC	DNC	DNC	DNC	DNC	DNC	DNC	DNC	DNC	DNC	DNC	DNC
Kv_tclc	$3.8x10^{-5}$	0.25	DNC	DNC	DNC	DNC	DNC	DNC	DNC	DNC	DNC	DNC	DNC	DNC
Kv_tclc	$7.7x10^{-5}$	0.5	-0.01	2.39	2.46	53206	50348	45431	45374	5057	1101	33690	13951	18337
Kv_tclc	$1.5x10^{-4}$	1	-0.29	2.39	2.99	53259	50462	46745	46687	8397	2628	32613	13868	18196
Kv_tclc	$7.7x10^{-4}$	5	-1.63	2.77	3.56	53477	50927	53007	52950	25423	13412	33491	13579	17491
Kv_tclc	$1.5x10^{-3}$	10	-2.52	3.32	4.21	53542	51169	57548	57492	38725	23042	33333	13329	16358

Table 3-6 (continued)

Parameter	Value	Factor of Basecase Values	Mean Error	Abs Mean Error	RMS	Flow (ft³/day) from lower face of bottom layer in hydrostratigraphic unit.						Baseflows (ft³/day)		
						"A horizon"	"AA horizon"	TZ	TCCZ	MAZ	TCLC	Joyce Branch	R-Effluent Canal	Mill Creek
Kv_tclc	3.1×10^{-3}	20	-3.57	4.09	5.09	53624	51457	63151	63096	56376	36321	33297	13329	16359
Kv_tclc	7.7×10^{-3}	50	DNC	DNC	DNC	DNC	DNC	DNC	DNC	DNC	DNC	DNC	DNC	DNC
Kv_laz	9.0×10^{-3}	0.1	-0.25	2.38	2.98	53255	50454	46632	46575	8164	2288	31563	13874	15389
Kv_laz	4.5×10^{-2}	0.5	-0.28	2.39	2.99	53260	50464	46763	46706	8436	2684	33639	13867	18193
Kv_laz	9.0×10^{-2}	1	-0.29	2.39	2.99	53259	50462	46745	46687	8397	2628	32613	13868	18196
Kv_laz	0.45	5	-0.29	2.39	2.99	53260	50464	46763	46406	8456	2684	33584	13867	18110
Kv_laz	0.90	10	-0.29	2.39	2.99	53260	50464	46766	46709	8442	2693	33639	13867	18106
Kh_a	4.1×10^{-2}	0.1	0.29	2.65	3.50	53857	50924	46894	46836	8416	2636	32470	13722	18110
Kh_a	0.21	0.5	-0.02	2.42	3.05	53570	50712	46828	46770	8407	2632	33619	13791	18151
Kh_a	0.41	1	-0.29	2.39	2.99	53259	50462	46745	46687	8397	2628	32613	13868	18196
Kh_a	0.51	1.25	-0.39	2.38	2.99	53117	50344	46704	46646	8302	2626	33647	13906	18218
Kh_a	0.62	1.5	-0.48	2.38	3.00	52981	50229	46664	46606	8387	2624	33656	13947	18234
Kh_a	2.1	5	DNC	DNC	DNC	DNC	DNC	DNC	DNC	DNC	DNC	DNC	DNC	DNC
Kh_a	4.1	10	DNC	DNC	DNC	DNC	DNC	DNC	DNC	DNC	DNC	DNC	DNC	DNC
Kh_aa3	3.8×10^{-2}	0.1	-0.28	2.40	3.00	53259	50465	46723	46665	8394	2627	33667	13864	18193
Kh_aa3	0.19	0.5	-0.28	2.39	2.99	53259	50465	46732	46675	8395	2627	33667	13865	18194
Kh_aa3	0.38	1	-0.29	2.39	2.99	53259	50462	46745	46687	8397	2628	32613	13868	18196
Kh_aa3	3.8	10	0.28	2.35	2.95	53265	50467	46816	46750	8405	2632	33668	13865	18194
Kh_aa3	19	50	-0.23	2.35	2.93	53276	50473	46910	46852	8417	2636	33669	13877	18238
Kh_tz	0.8	0.1	DNC	DNC	DNC	DNC	DNC	DNC	DNC	DNC	DNC	DNC	DNC	DNC
Kh_tz	1	0.1	DNC	DNC	DNC	DNC	DNC	DNC	DNC	DNC	DNC	DNC	DNC	DNC
Kh_tz	4	0.5	0.53	2.53	3.14	53017	49861	48883	48825	8685	2740	26138	13851	12135
Kh_tz	8	1	-0.29	2.39	2.99	53259	50462	46745	46687	8397	2628	32613	13868	18196
Kh_tz	12	1.5	-0.78	2.36	3.05	53363	50761	45402	45345	8223	2559	41072	13919	23935
Kh_tz	30	3.8	-1.74	2.62	3.45	53562	51272	42774	42717	7891	2428	74387	14031	48656
Kh_tz	80	10	-2.37	3.01	3.89	53625	51552	34922	34865	7661	2361	166614	14140	115674
Kh_maz	2	0.1	2.46	3.21	3.95	52542	48697	28922	28858	10142	3194			
Kh_maz	10	0.5	0.80	2.49	3.07	52997	49826	40119	40059	9127	2889	32613	14333	18933
Kh_maz	20	1	-0.29	2.39	2.99	53259	50462	46745	46687	8397	2628	32613	13868	18196
Kh_maz	30	1.5	-0.95	2.46	3.16	53396	50753	50614	50558	7844	2460			
Kh_maz	50	2.5	-1.74	2.79	3.58	53508	51023	55055	55000	7411	2260			
Kh_maz	200	10	-3.07	3.63	4.56	53606	51369	63138	63085	6461	1899	33450	13367	16593
Kh_laz	3	0.1	-0.21	2.40	2.97	53255	50455	46662	46605	8228	2265	33639	13848	18206
Kh_laz	15	0.5	-0.28	2.39	2.98	53259	50461	46733	46676	8373	2579	33009	13869	18196
Kh_laz	30	1	-0.29	2.39	2.99	53259	50462	46745	46687	8397	2628	32613	13868	18196
Kh_laz	150	5	-1.29	2.39	2.99	53260	50463	46756	46698	8419	2675	33639	13868	18213
Kh_laz	300	10	-0.30	2.39	2.99	53260	50463	46758	46700	8426	2683	33639	13868	18194

3.9 Remedial Alternative Flow Fields

Upon completion of the calibrated groundwater flow field, which was based on the current conditions and the presence of the existing asphalt cover, additional flow fields were developed for the different basin cover scenarios (remedial alternatives). The flow fields for the remedial alternatives used the same parameter dataset as the calibrated flow field, with two exceptions. First, recharge through the basin cover was varied for each remedial alternative and second, the areal extent of the basin cover was increased for the 15-acre cover alternatives. The recharge rate for each of the remedial alternatives, based on basin cover, was discussed in Section 1.4.

The simulated potentiometric surfaces in the "A" horizon (water-table aquifer) were developed for each remedial alternative: Failed Asphalt Cover (Figure 3-30); $1x10^{-5}$ cm/s Soil Cover with the existing cover footprint (Figure 3-31); $1x10^{-5}$ cm/s Soil Cover with the 15-acre cover (Figure 3-32), Concrete Cover with the 15-acre cover (Figure 3-33); and the Reinforced Asphalt Cover with the 15-acre cover (Figure 3-34). For the Failed Asphalt Cover, it was assumed that at the present time, the integrity of the asphalt cover degraded to a condition where 50% of the background recharge was allowed through the cover. This assumption resulted in an applied recharge of 7.5 in/yr to the water table through the asphalt cover. As a result of the increased recharge through the footprint of the existing asphalt cover, higher water levels, with maximum elevations of 292 ft near the southeastern corner of the asphalt cover, were observed (Figure 3-30).

The potentiometric surface for the $1x10^{-5}$ cm/s Soil Cover with the existing cover footprint (Figure 3-31) is based on a recharge through the cover of 6.2 in/yr. This flow field shows higher heads than the Existing Asphalt Cover and slightly lower heads than the Failed Asphalt Cover scenario. Figure 3-32 presents the potentiometric surface for the $1x10^{-5}$ cm/s Soil Cover with the 15-acre cover footprint. As compared to the small footprint simulation (Figure 3-31), the surface is similar with a decrease in the heads simulated in the vicinity of the additional cover to the south of Basin 6.

The potentiometric surface for the Concrete and the Reinforced Asphalt Covers with the 15-acre cover footprint are shown in Figures 3-33 and 3-34, respectively. These two surfaces show maximum heads lower than the $1x10^{-5}$ cm/s Soil Cover with the 15-acre cover footprint. This is expected given the lower recharge rates through the cover. However, these surfaces also show maximum heads and overall lower heads than the Existing Asphalt Cover (Figure 3-10). This difference is a result of the larger cover footprint. Areas previously subjected to ambient recharge (15 in/yr), especially to the south of Basin 6, were covered and assigned values five to 15 times smaller, thereby causing a depression in the water table underneath the cover.

A steady-state flow field was developed for each of the five remedial alternatives under evaluation. These flow fields, along with the Existing Asphalt Cover flow field, were used in the development of the contaminant transport models for the remedial alternative evaluation, as described in Section 4.0.

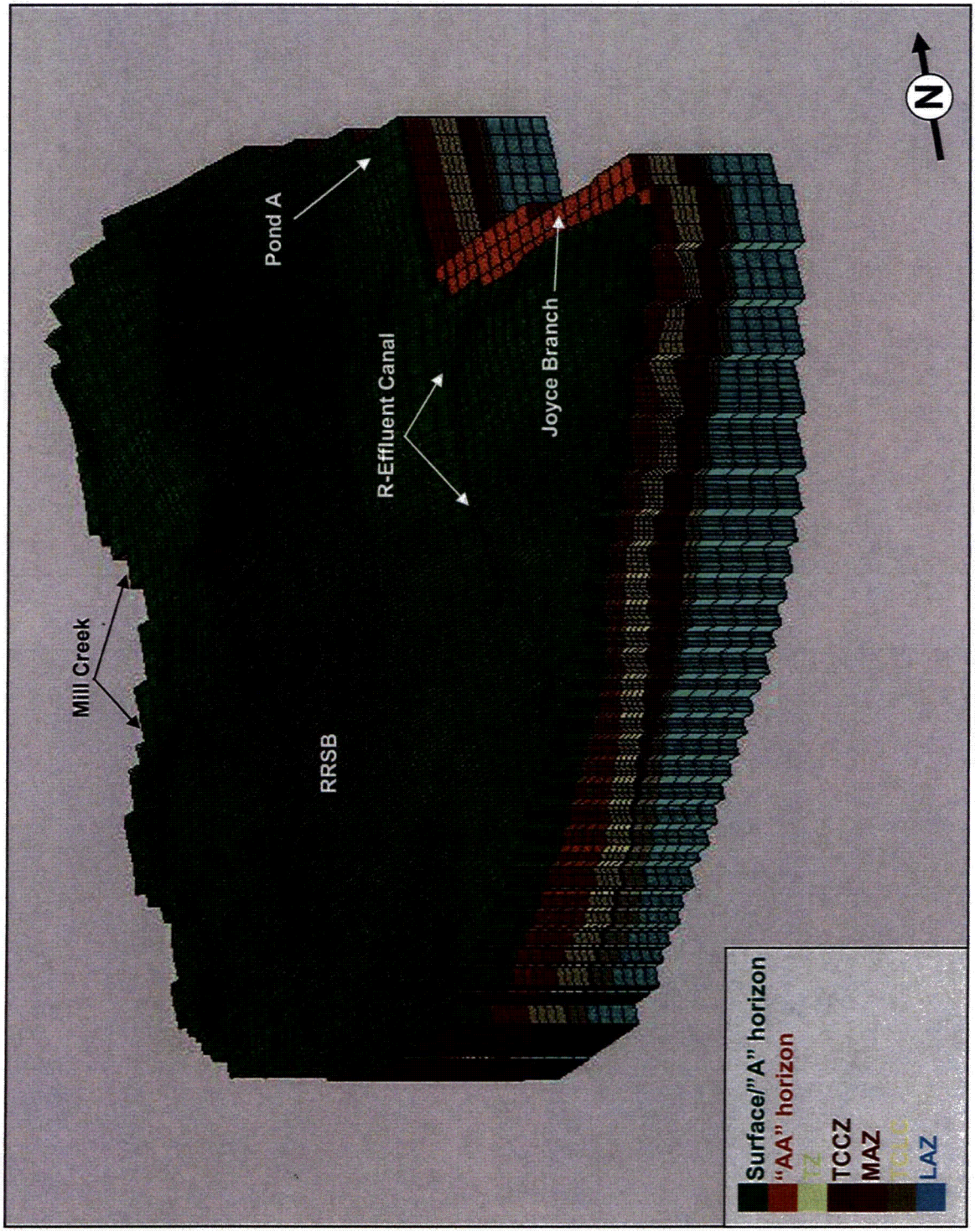

Figure 3-1. Model domain for the saturated-zone flow and transport models.

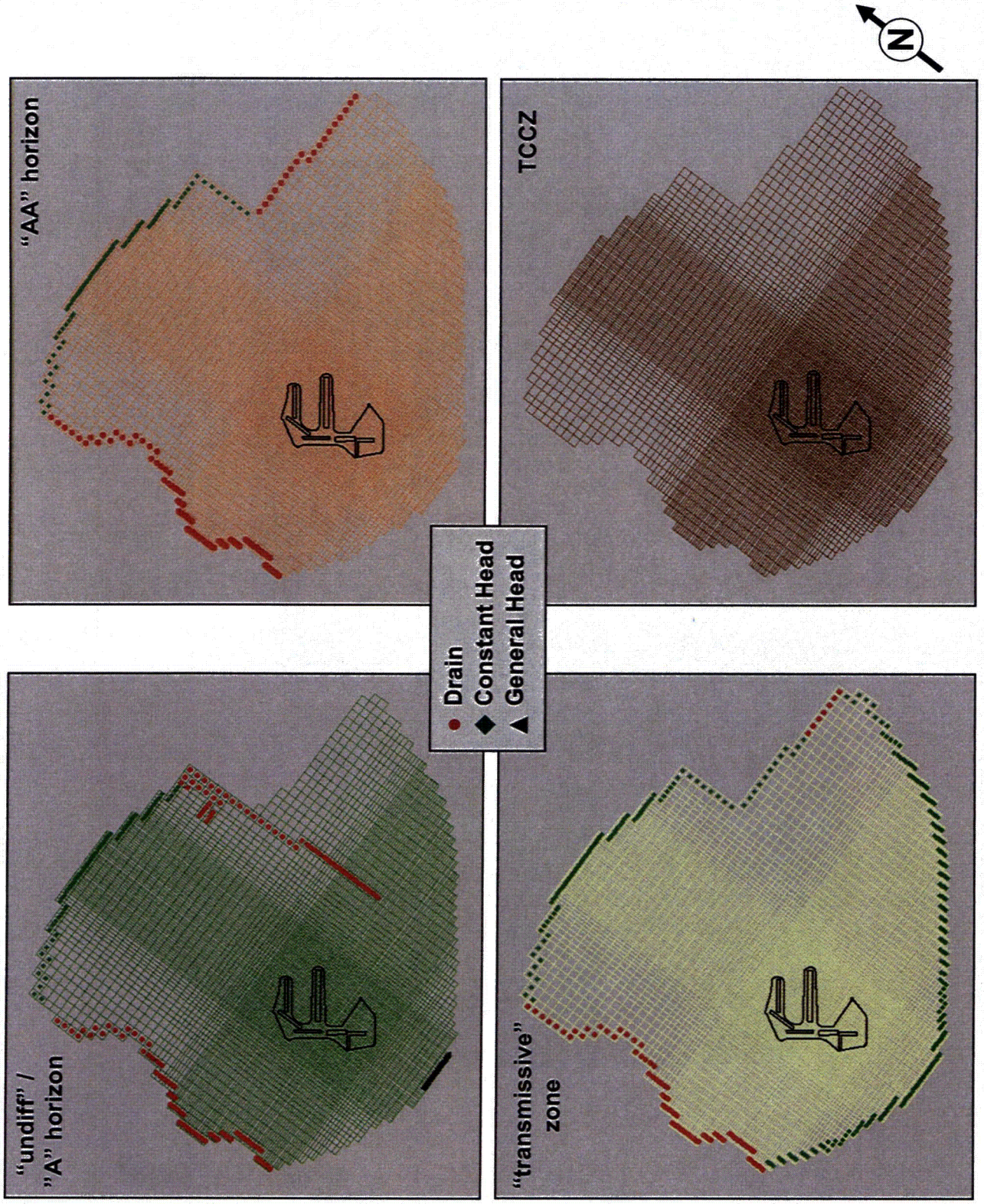

Figure 3-2a. Lateral boundary conditions for the saturated-zone flow model.

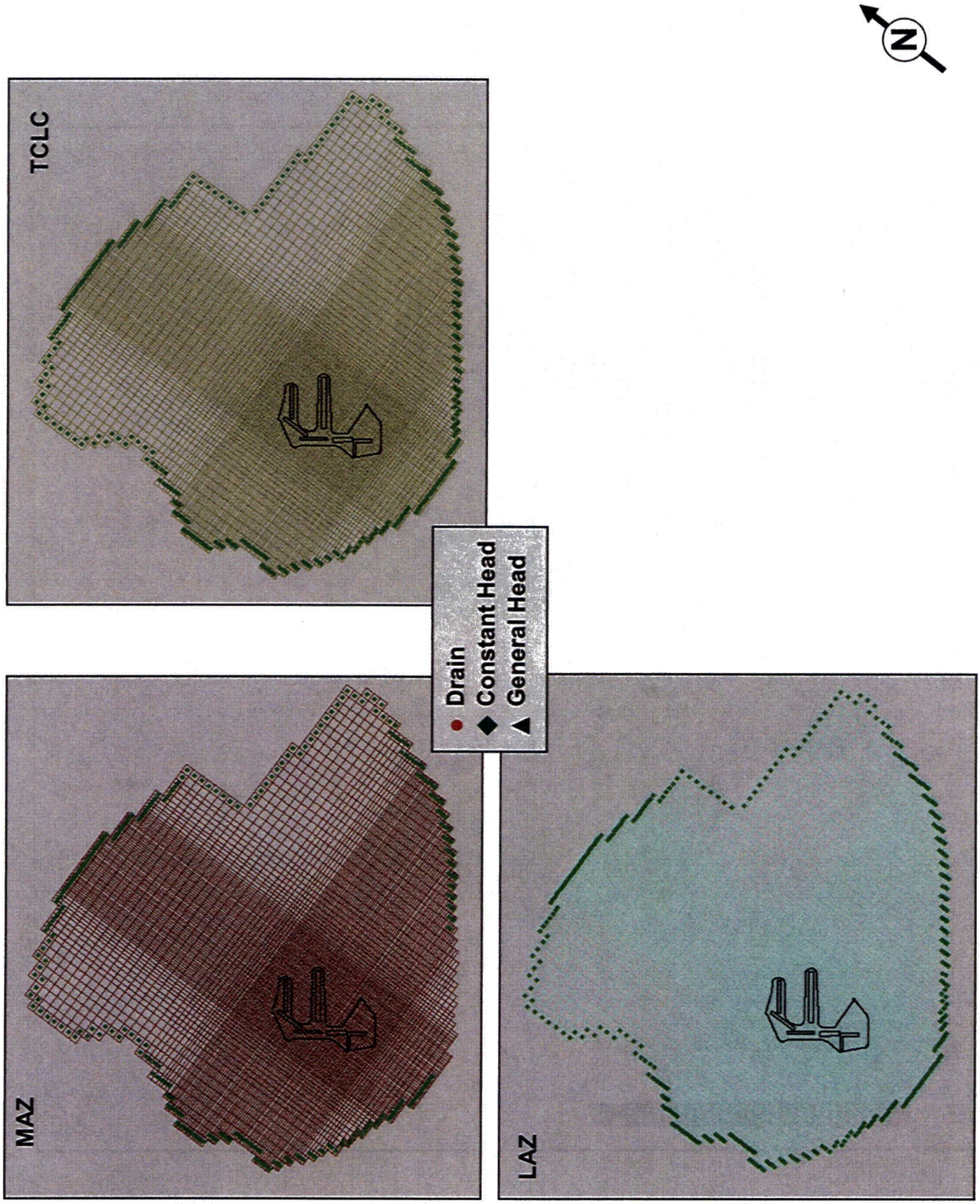

Figure 3-2b. Lateral boundary conditions for the saturated-zone flow model.

Figure 3-3. Average interpolated water-table surface for the "undifferentiated", "A", and "AA" soil horizons.

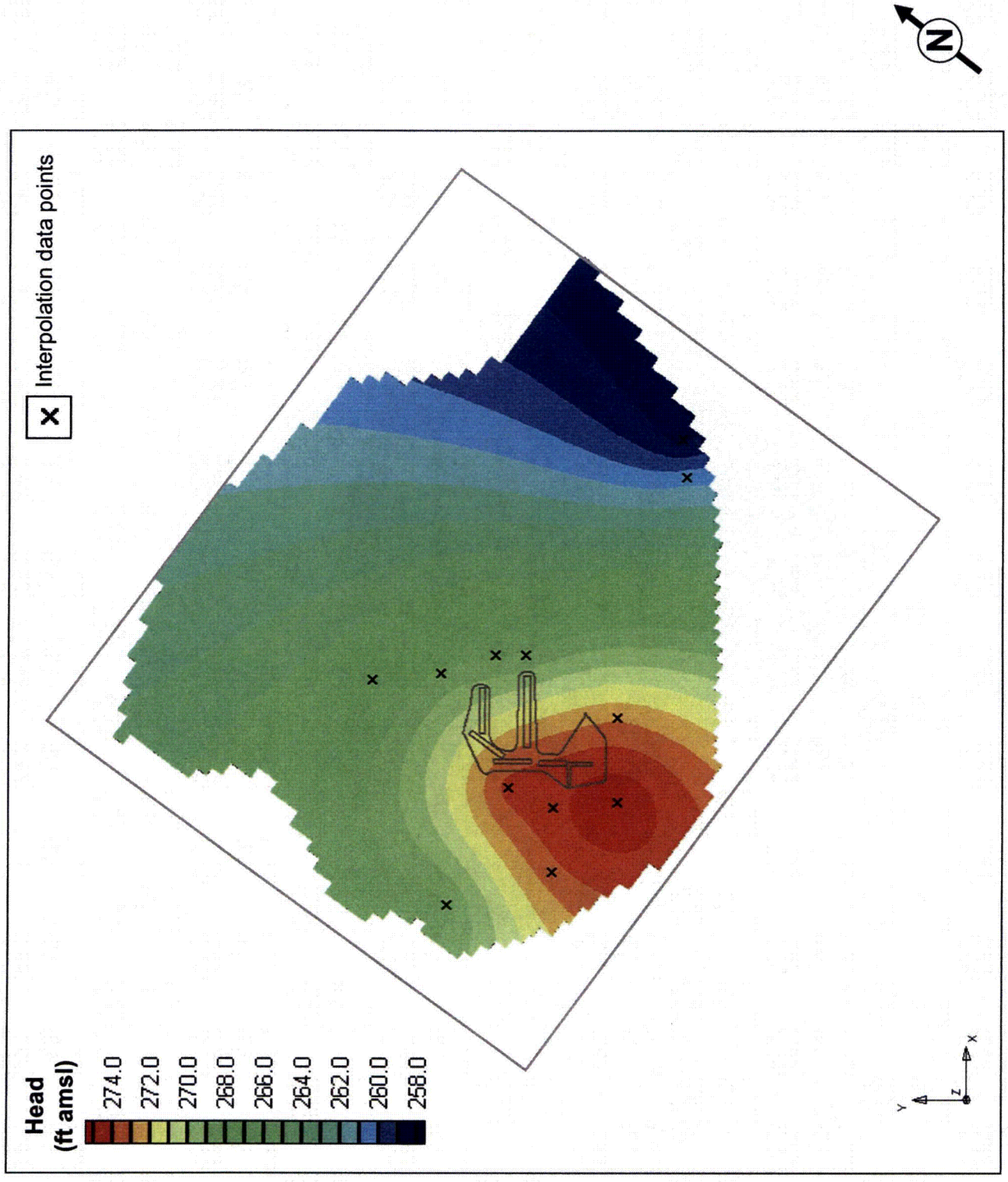

Figure 3-4. Average interpolated potentiometric surface for the TZ.

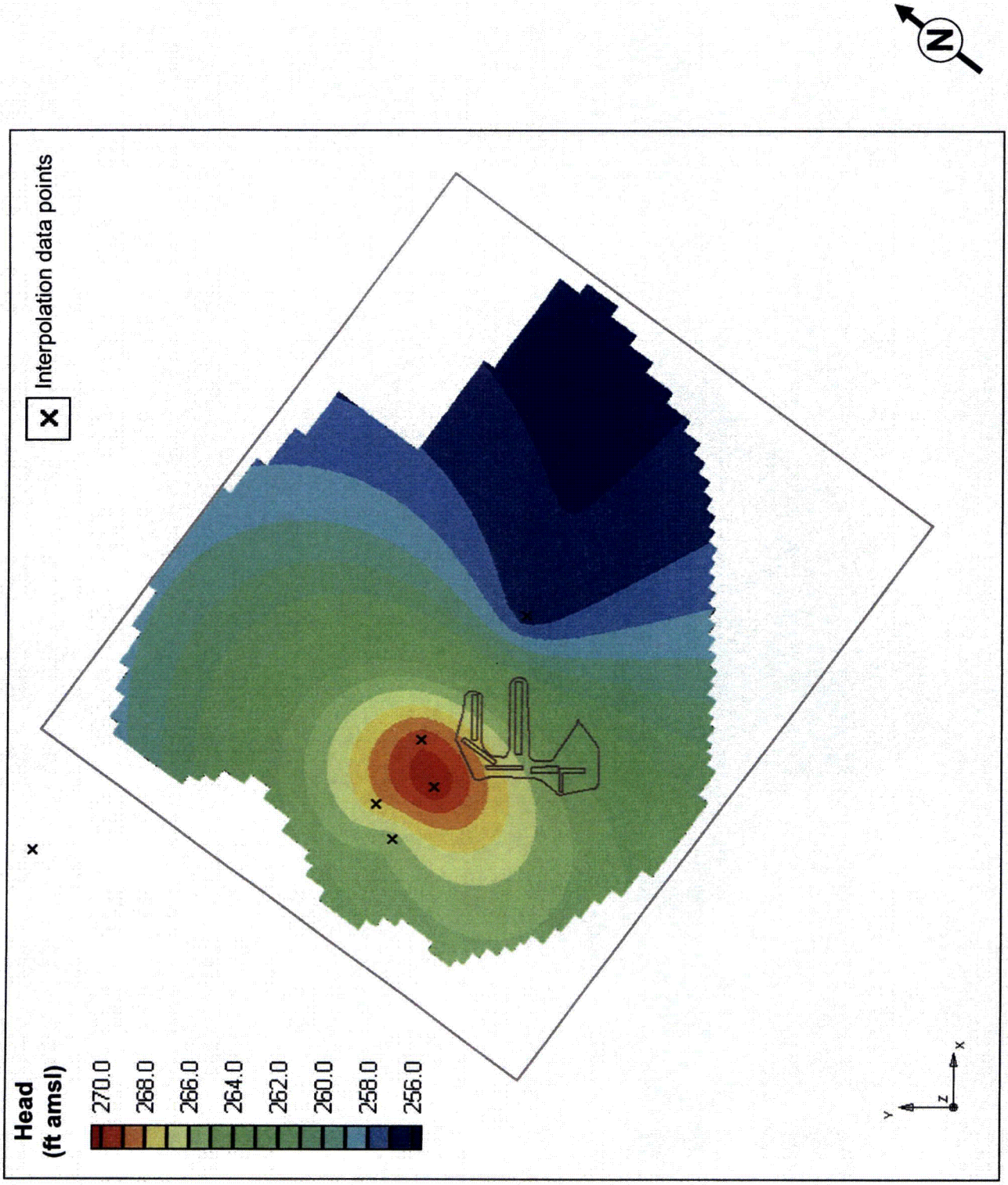

Figure 3-5. Average interpolated potentiometric surface for the MAZ.

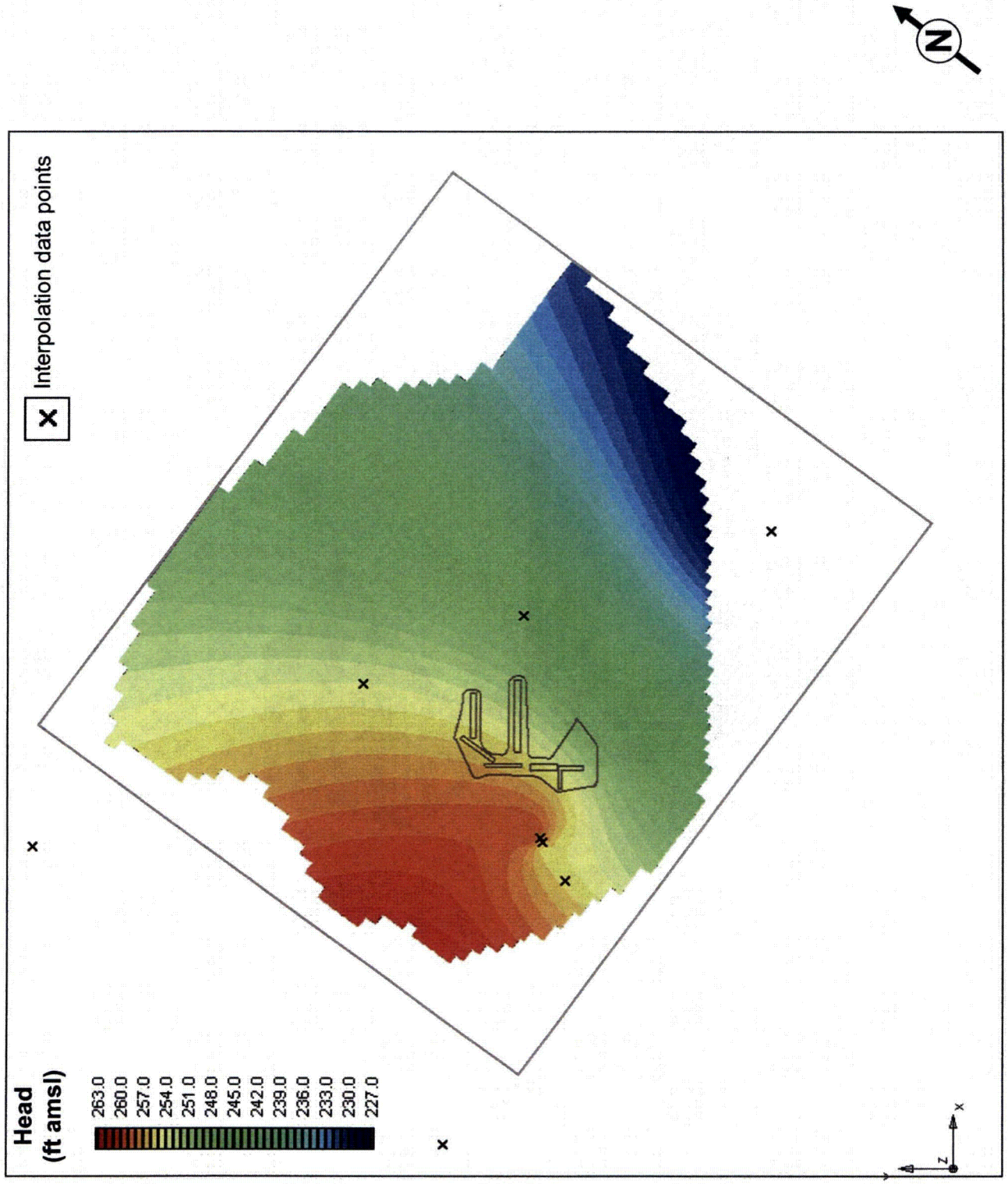

Figure 3-6. Average interpolated potentiometric surface for the LAZ.

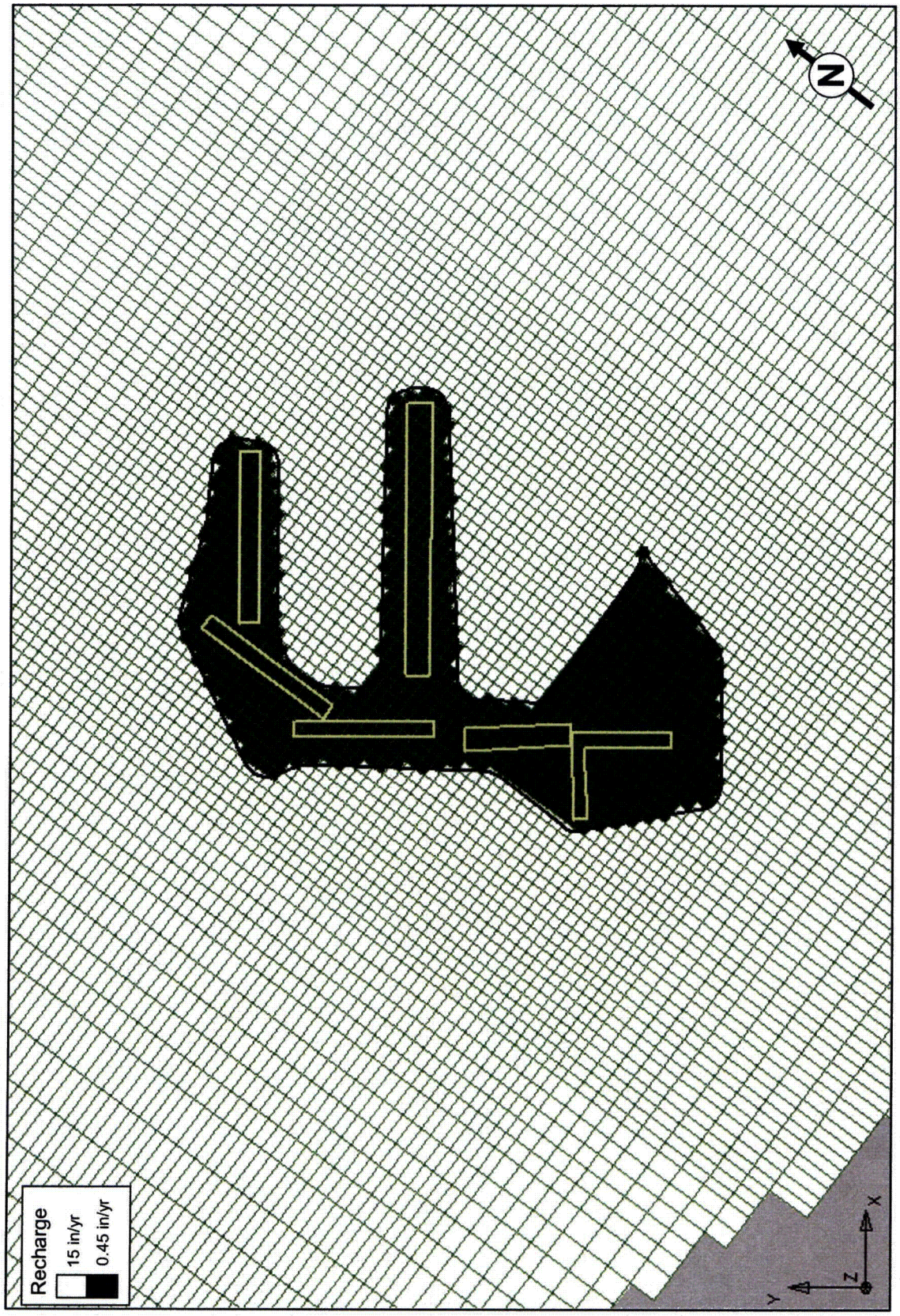

Figure 3-7. Model recharge to the uppermost saturated cells for the saturated-zone flow model for the condition of the existing asphalt cap.

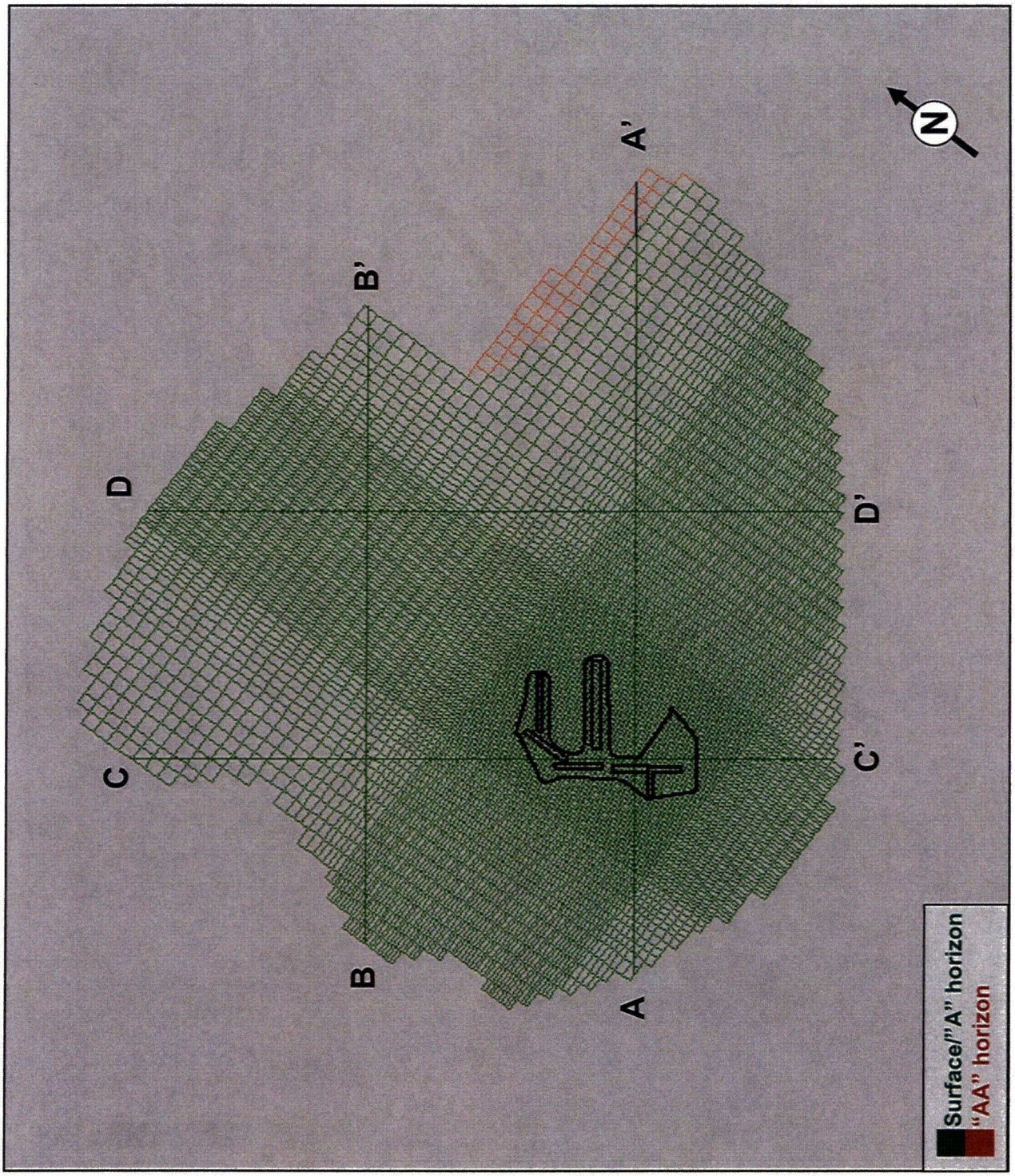

Figure 3-8. Lateral model grid for the saturated-zone flow and transport models showing cross-section locations.

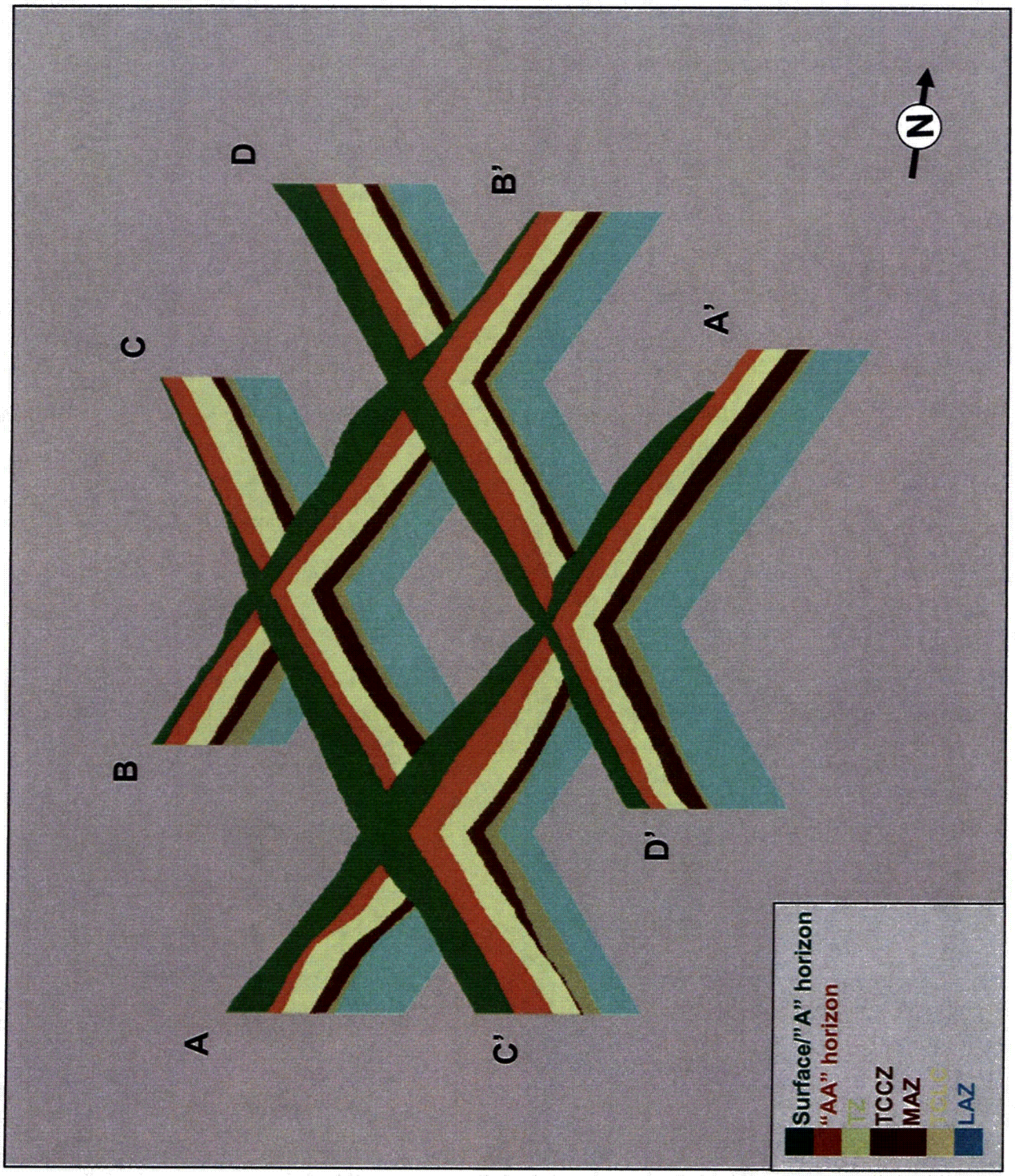

Figure 3-9. Oblique view of cross sections through the model grid for the saturated-zone flow and transport models.

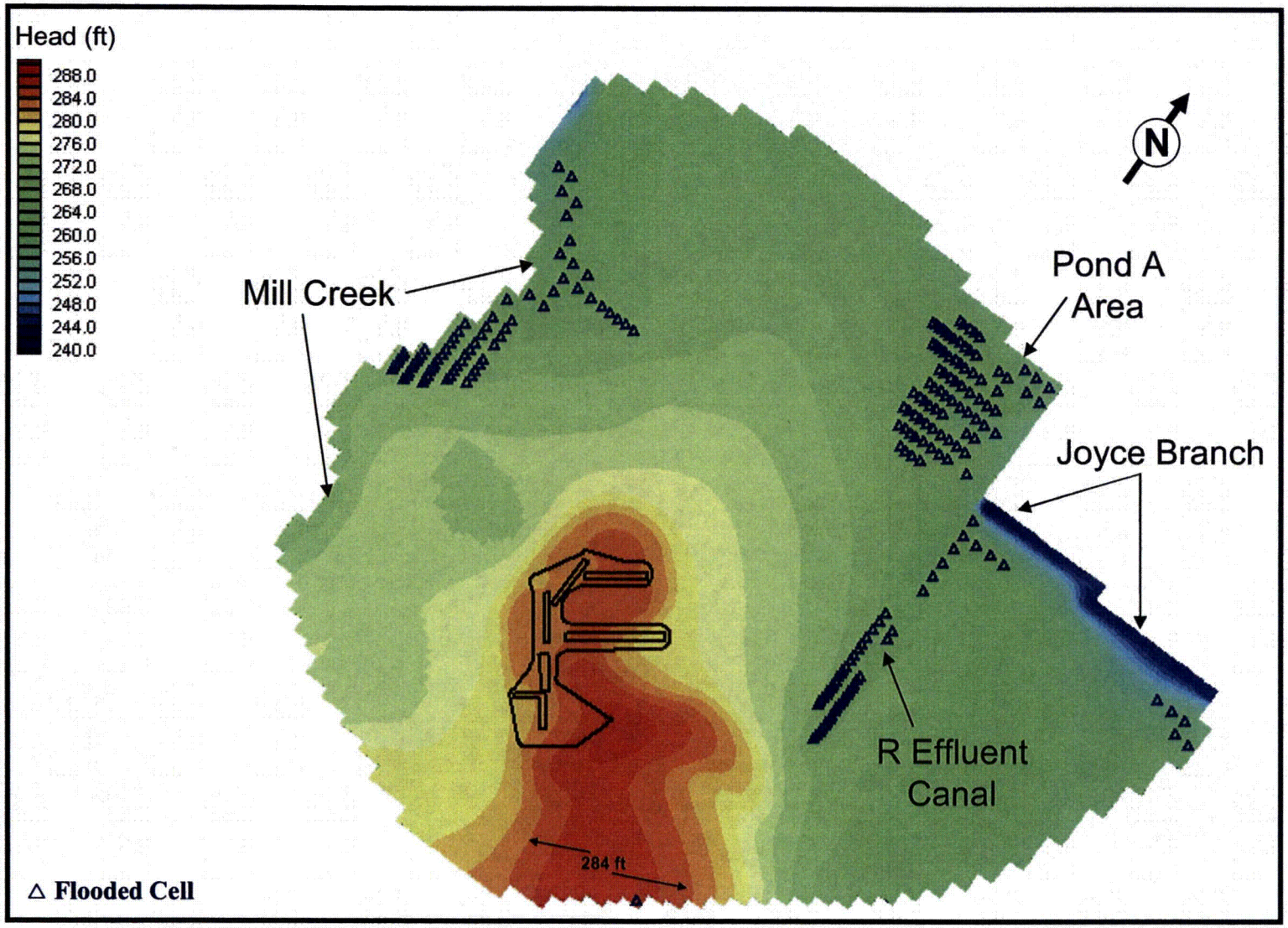

Figure 3-10. Water-table surface (combined "A" and "AA" soil horizons) for the calibrated saturated-zone flow model using the existing asphalt cover.

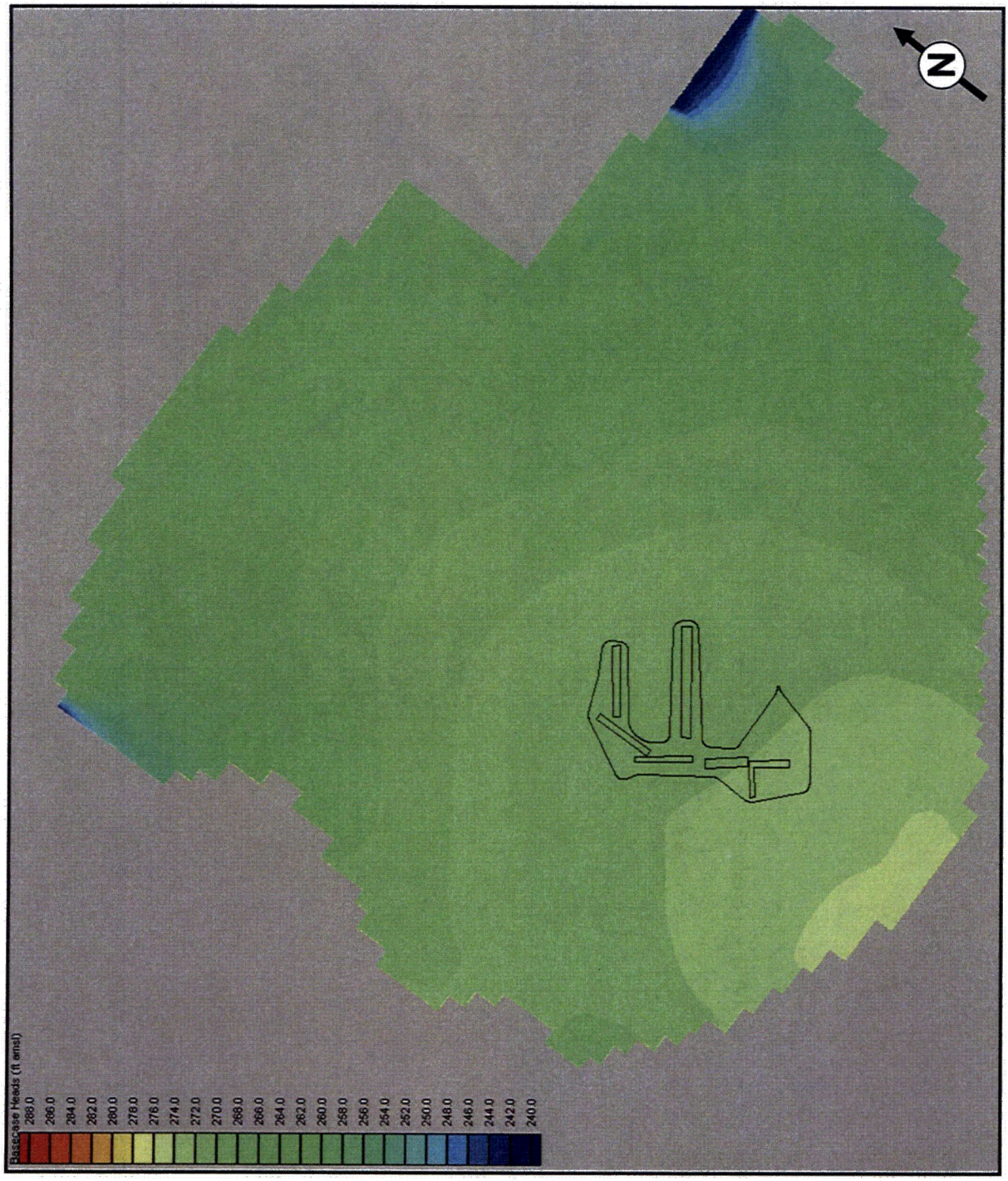

Figure 3-11. TZ potentiometric surface for the calibrated saturated-zone flow model.

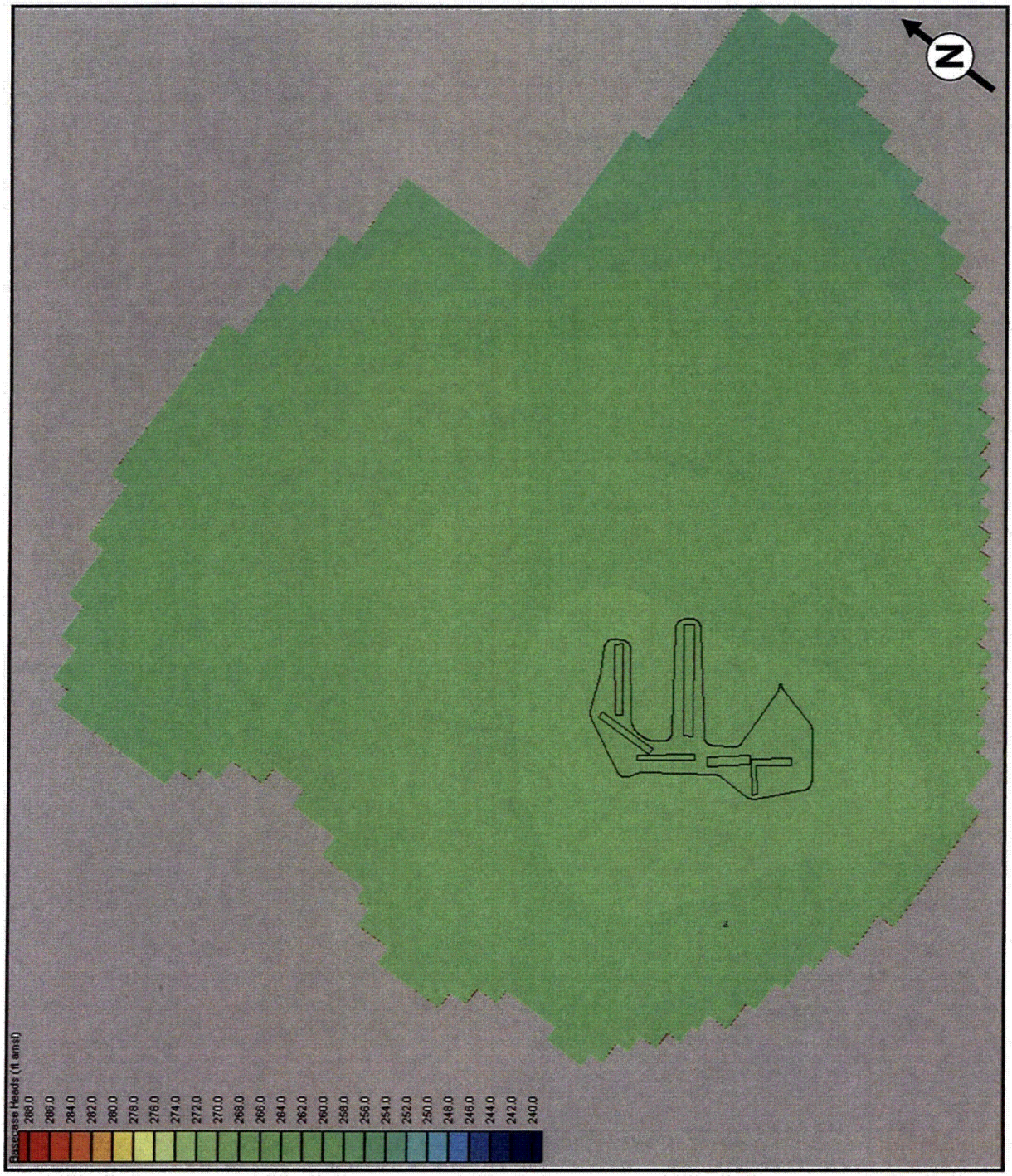

Figure 3-12. MAZ potentiometric surface for the calibrated saturated-zone flow model.

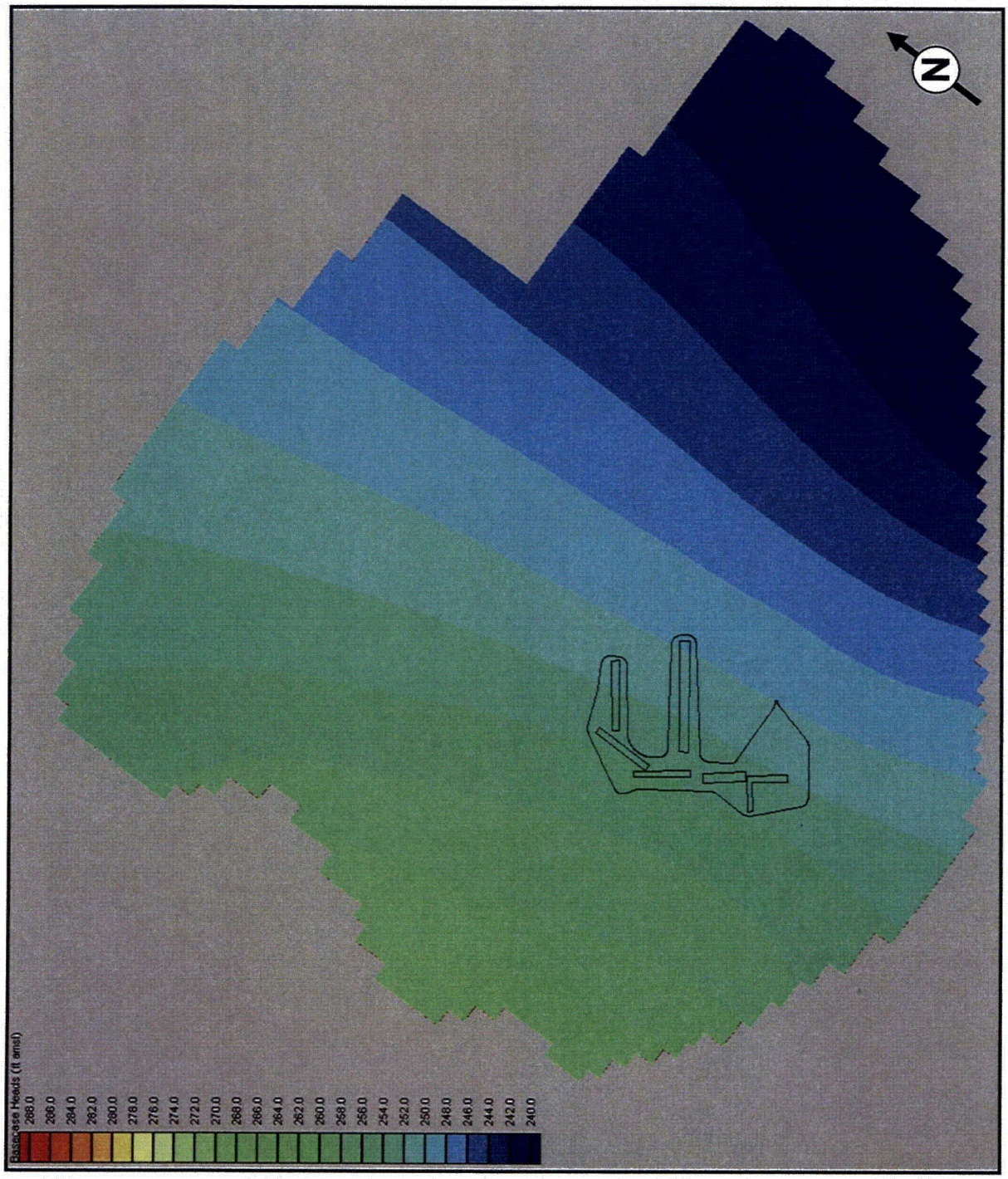

Figure 3-13. LAZ potentiometric surface for the calibrated saturated-zone flow model.

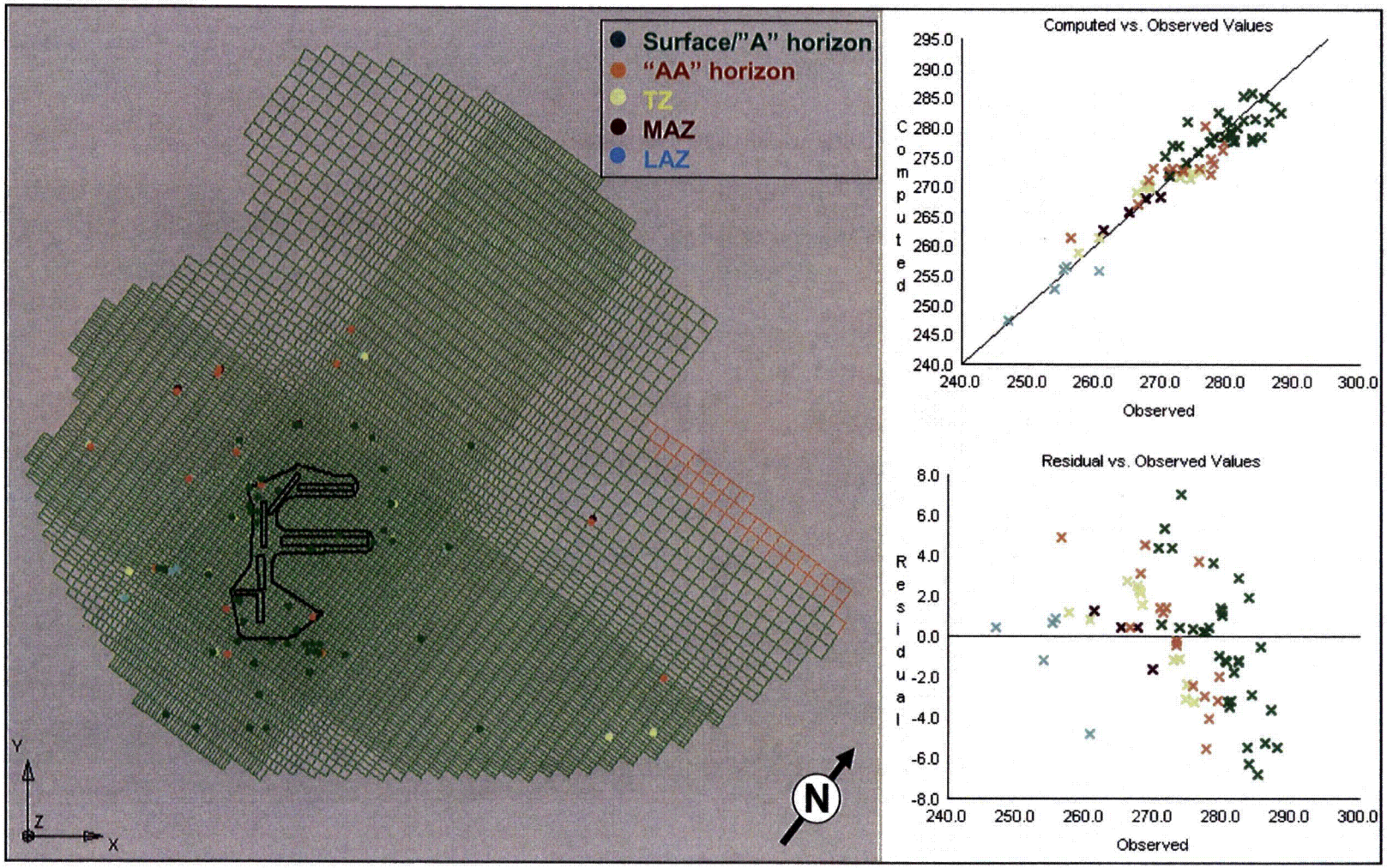

Figure 3-14. Computed heads versus observed heads and residual versus observed heads for the calibrated saturated-zone flow model.

Note: Elevation contours correspond to the bottom structure of the hydrostratigraphic layers.

Figure 3-15. Hydraulic conductivity zones in the "A" and "AA" horizons.

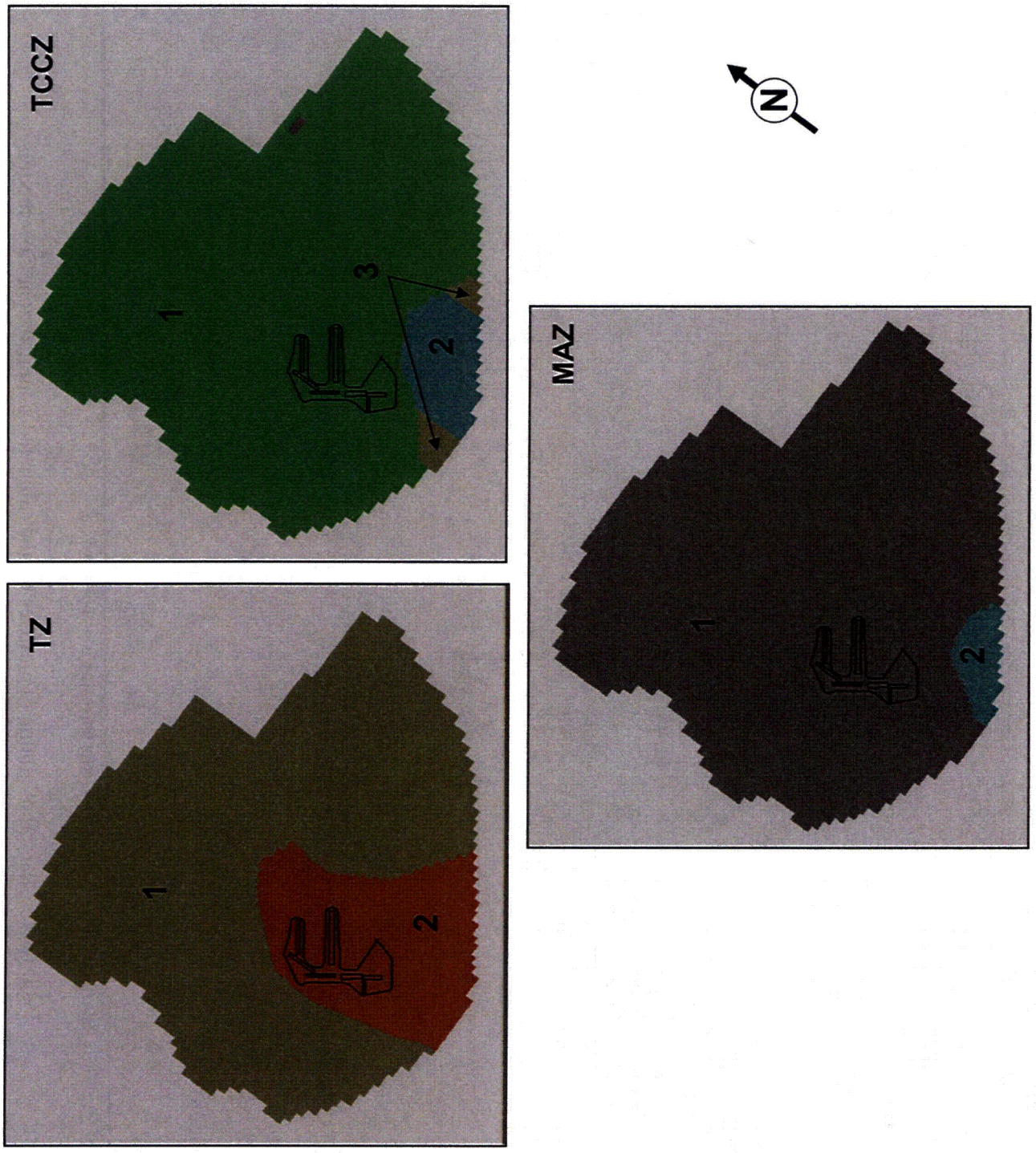

Figure 3-16. Hydraulic conductivity zones in the TZ, TCCZ, and MAZ.

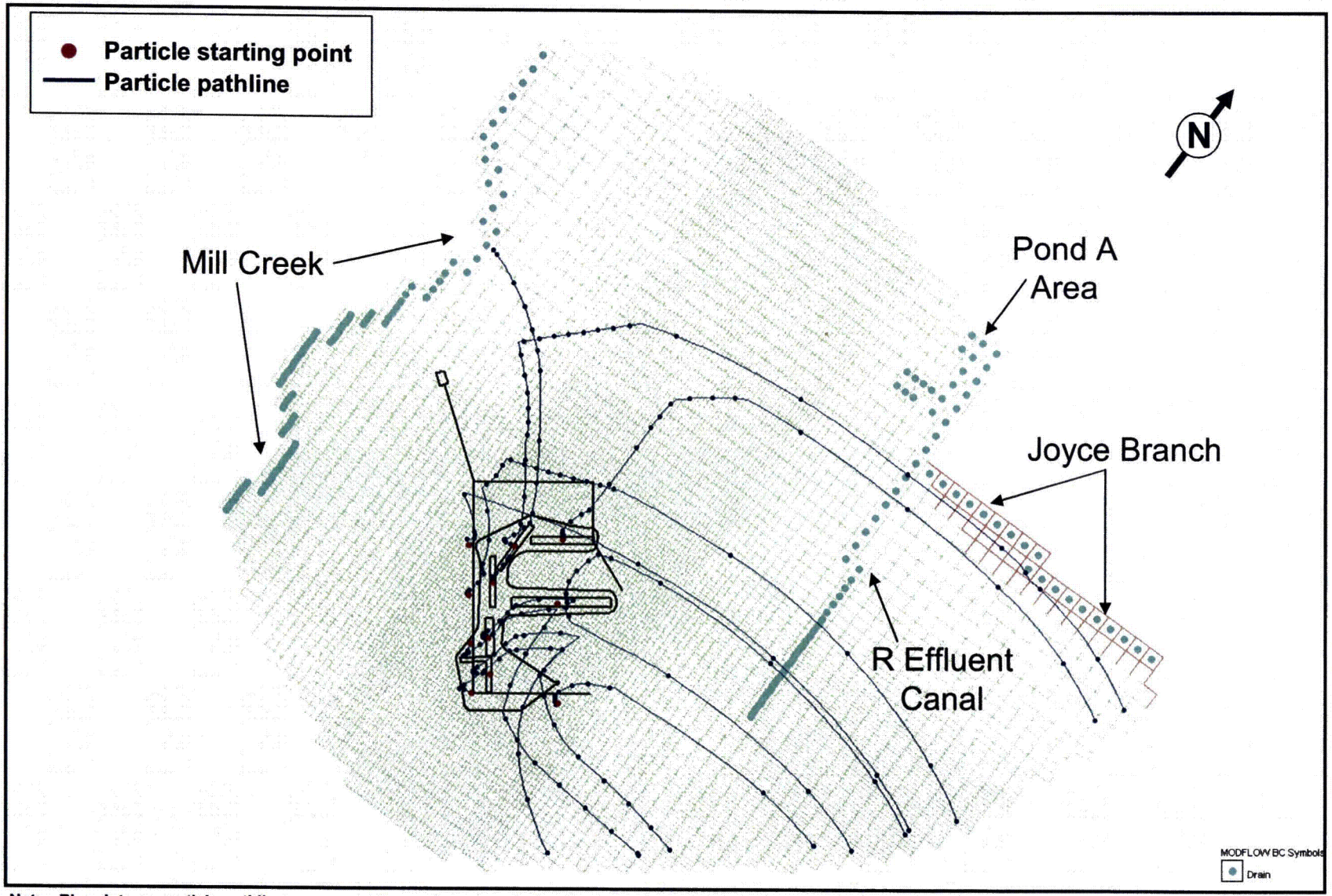

Note: Blue dots on particle pathlines represent 5-year time steps (advective transport only)

Figure 3-17. Lateral migration of particles for the calibrated saturated-zone flow model.

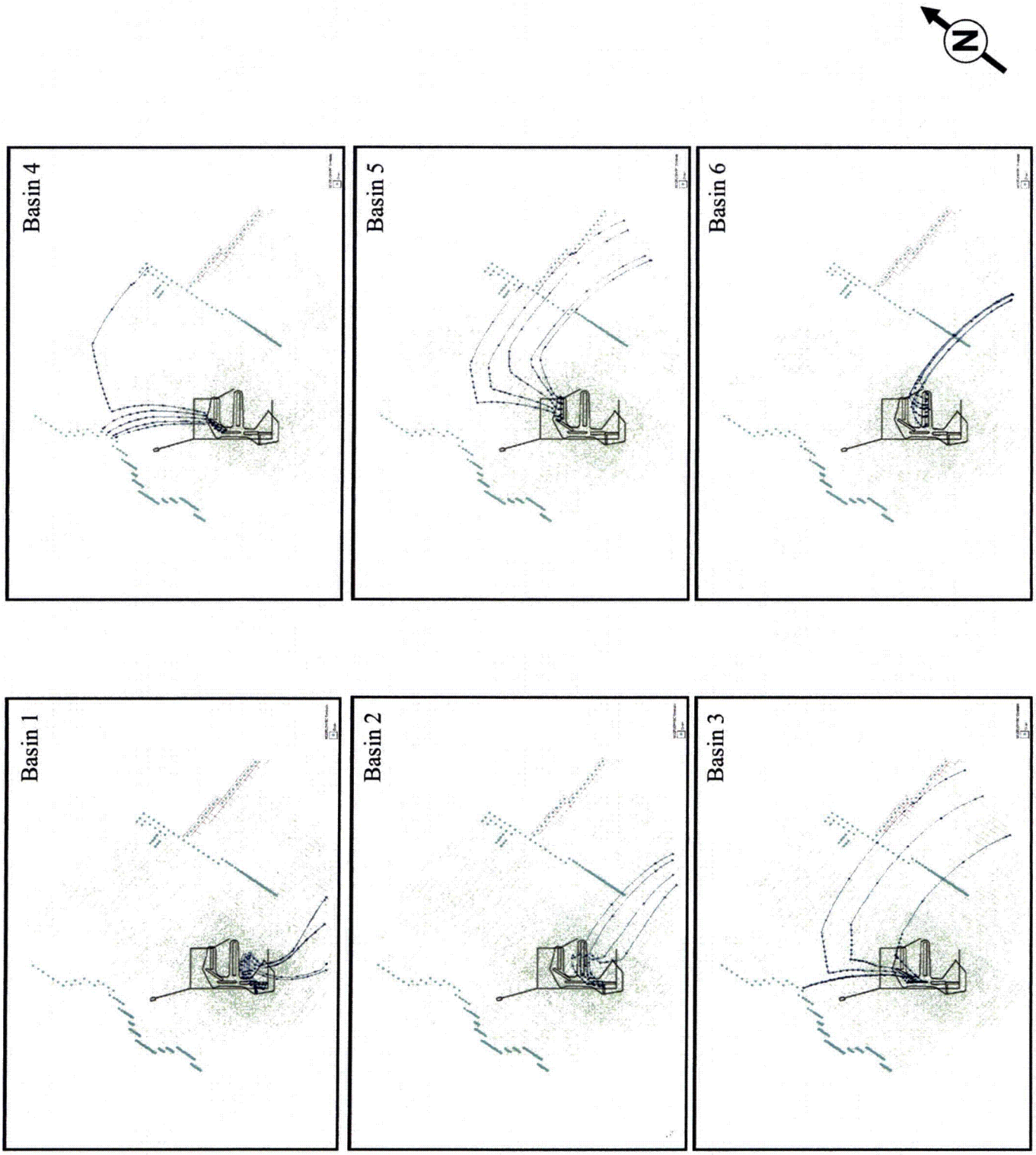

Figure 3-18. Lateral migration of particles released from each of the six seepage basins.

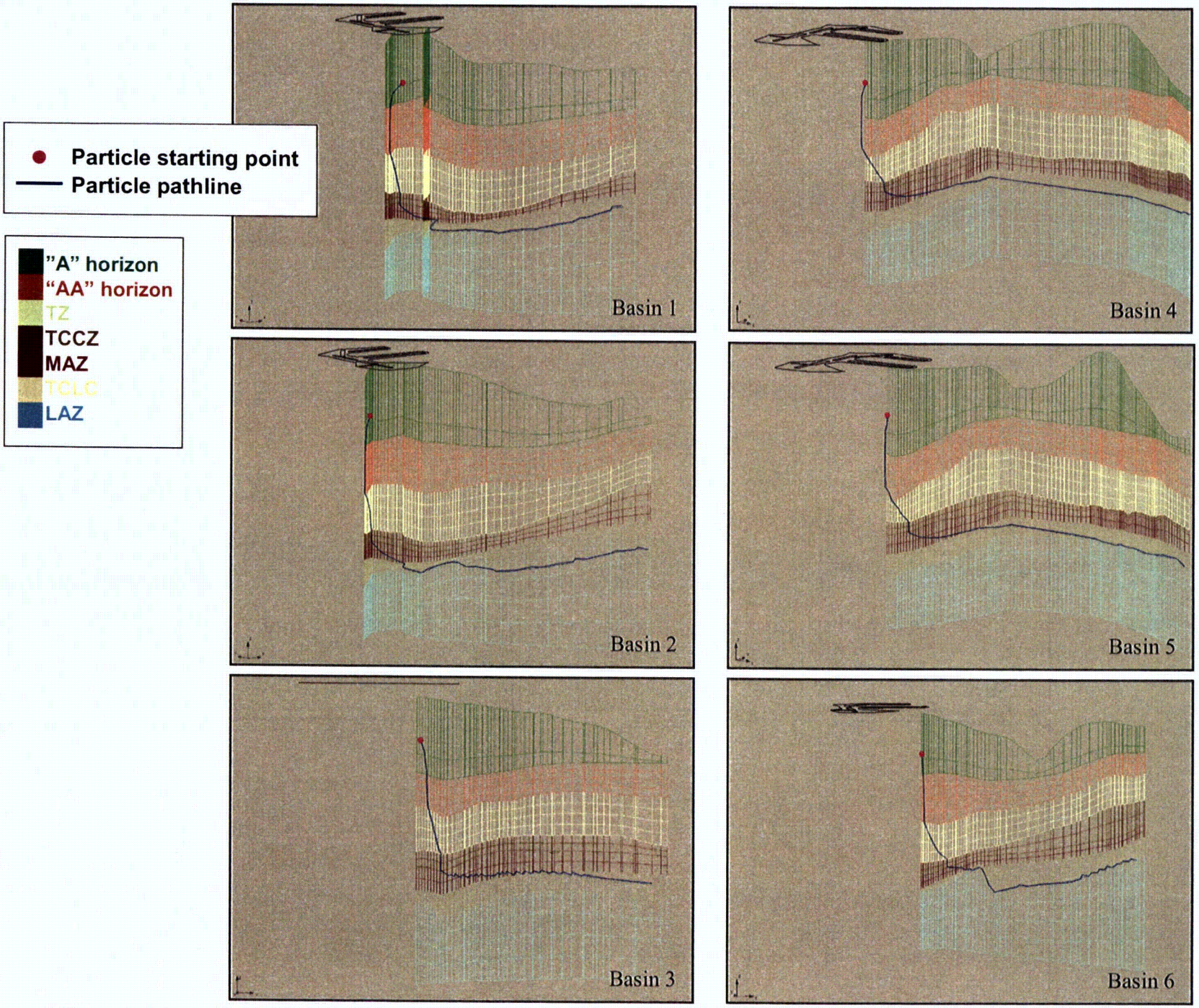

Figure 3-19. Particle pathlines along cross sections created for selected particles released from each of the six seepage basins.

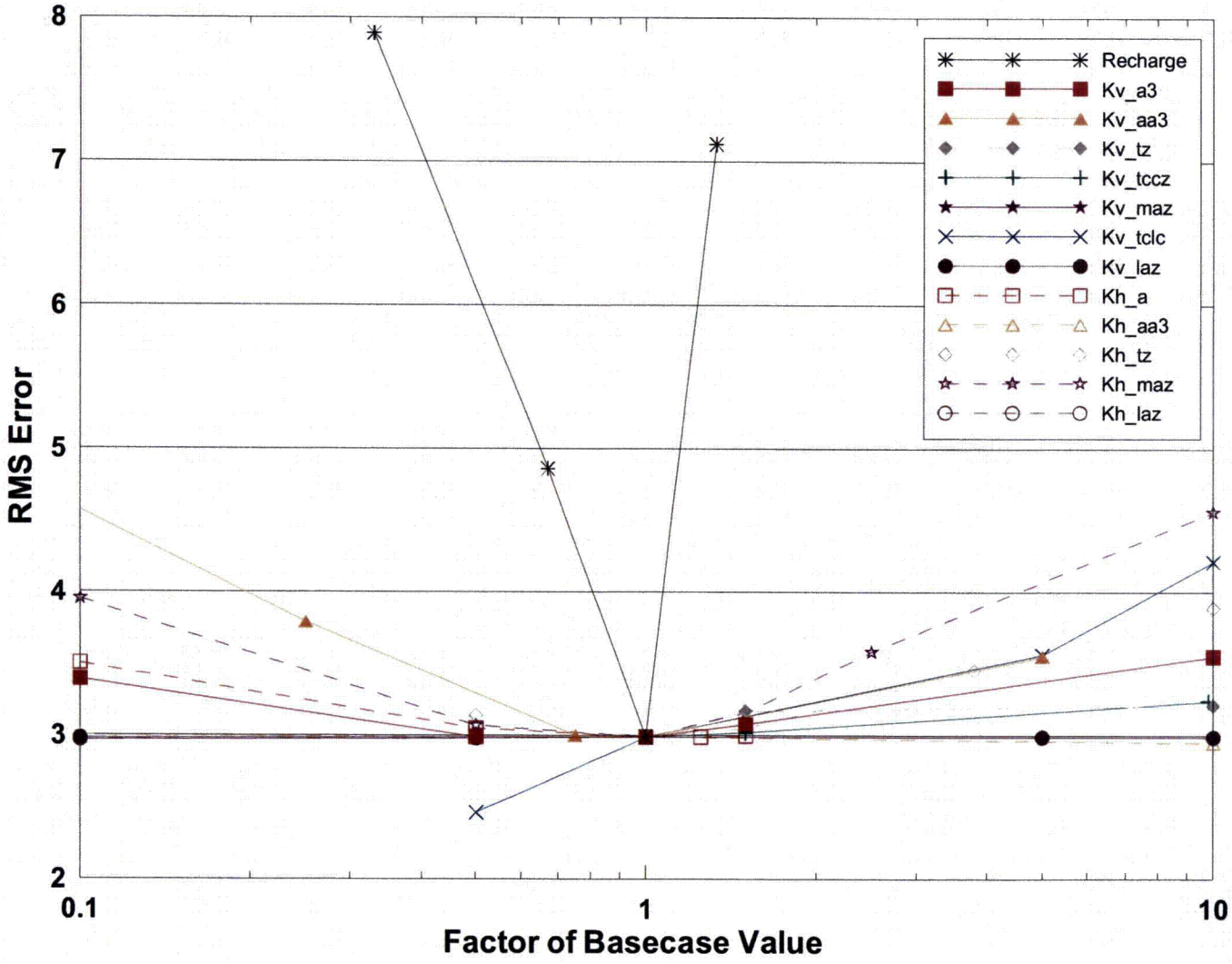

Figure 3-20. Sensitivity of root mean squared error.

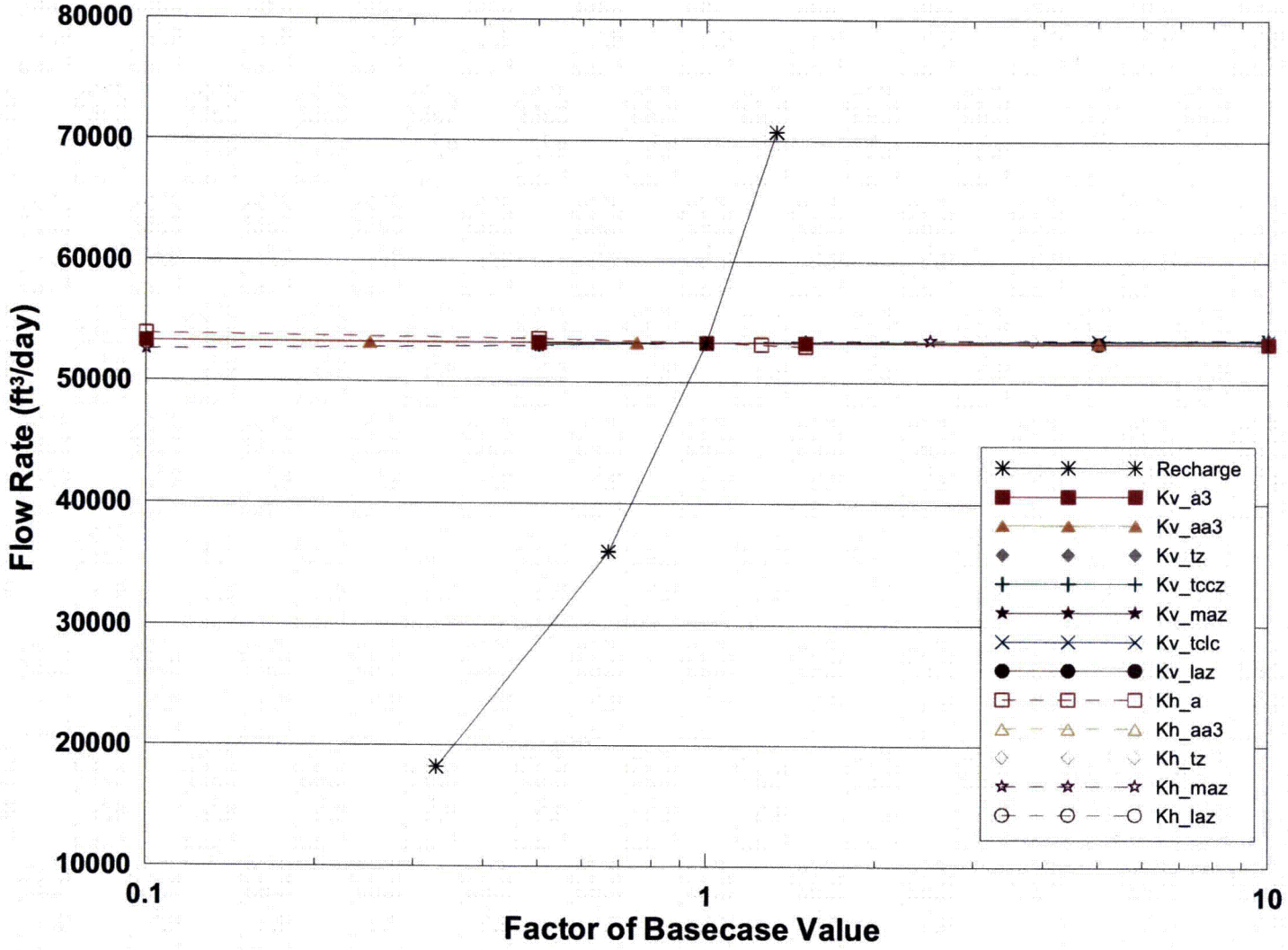

Figure 3-21. Changes in downward flow from "A" horizon.

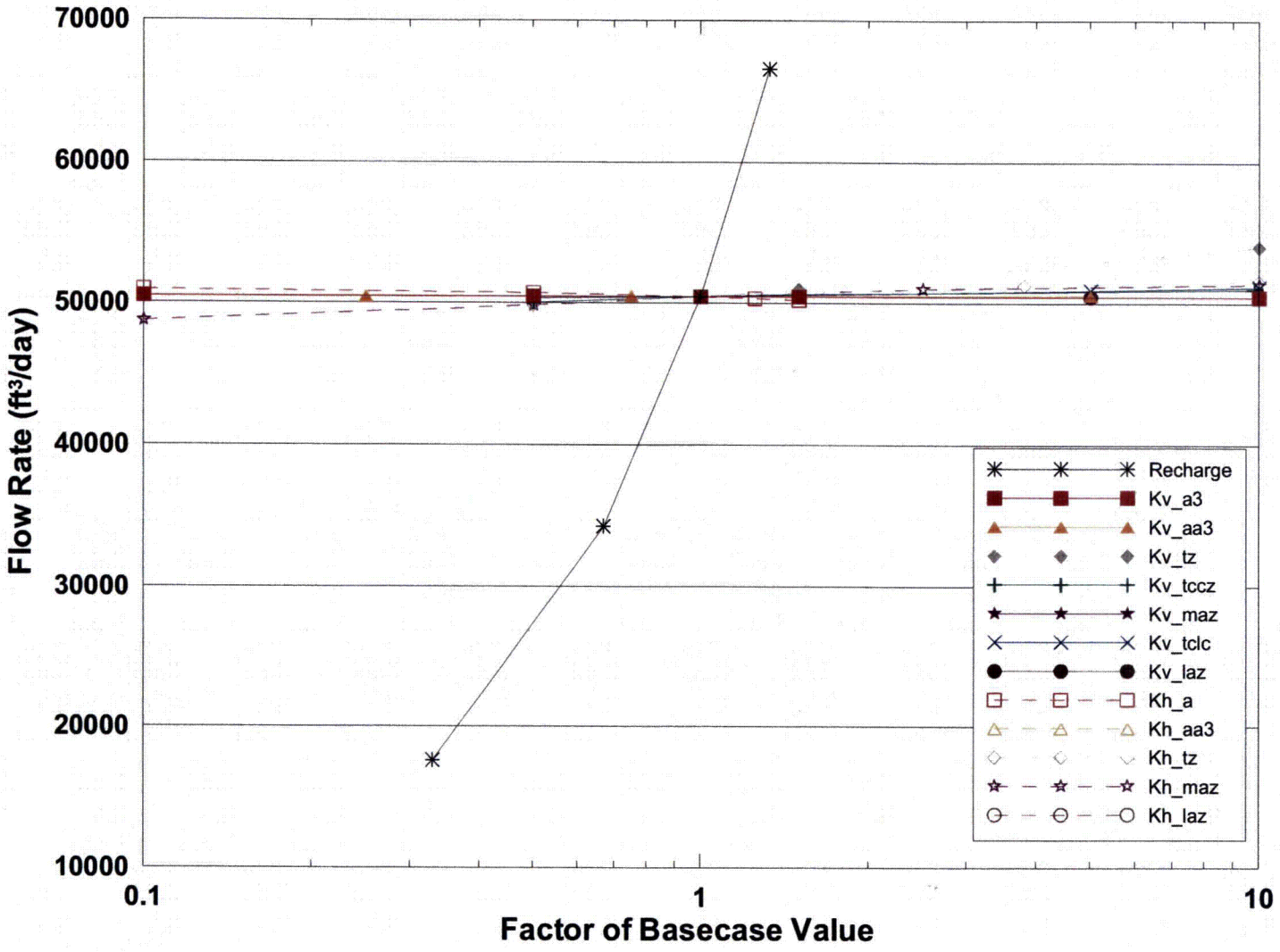

Figure 3-22. Changes in downward flow from "AA" horizon.

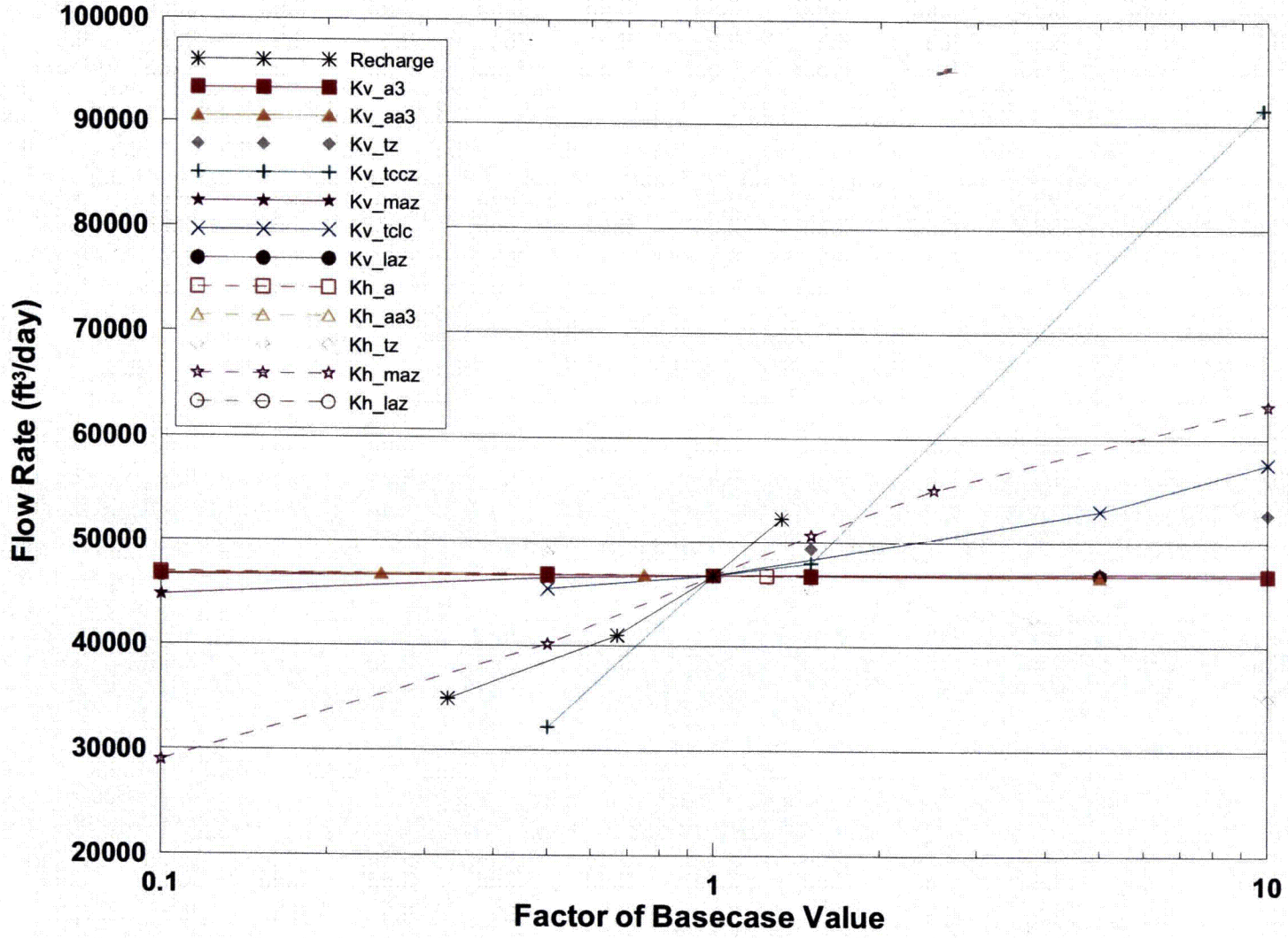

Figure 3-23. Changes in downward flow from TZ.

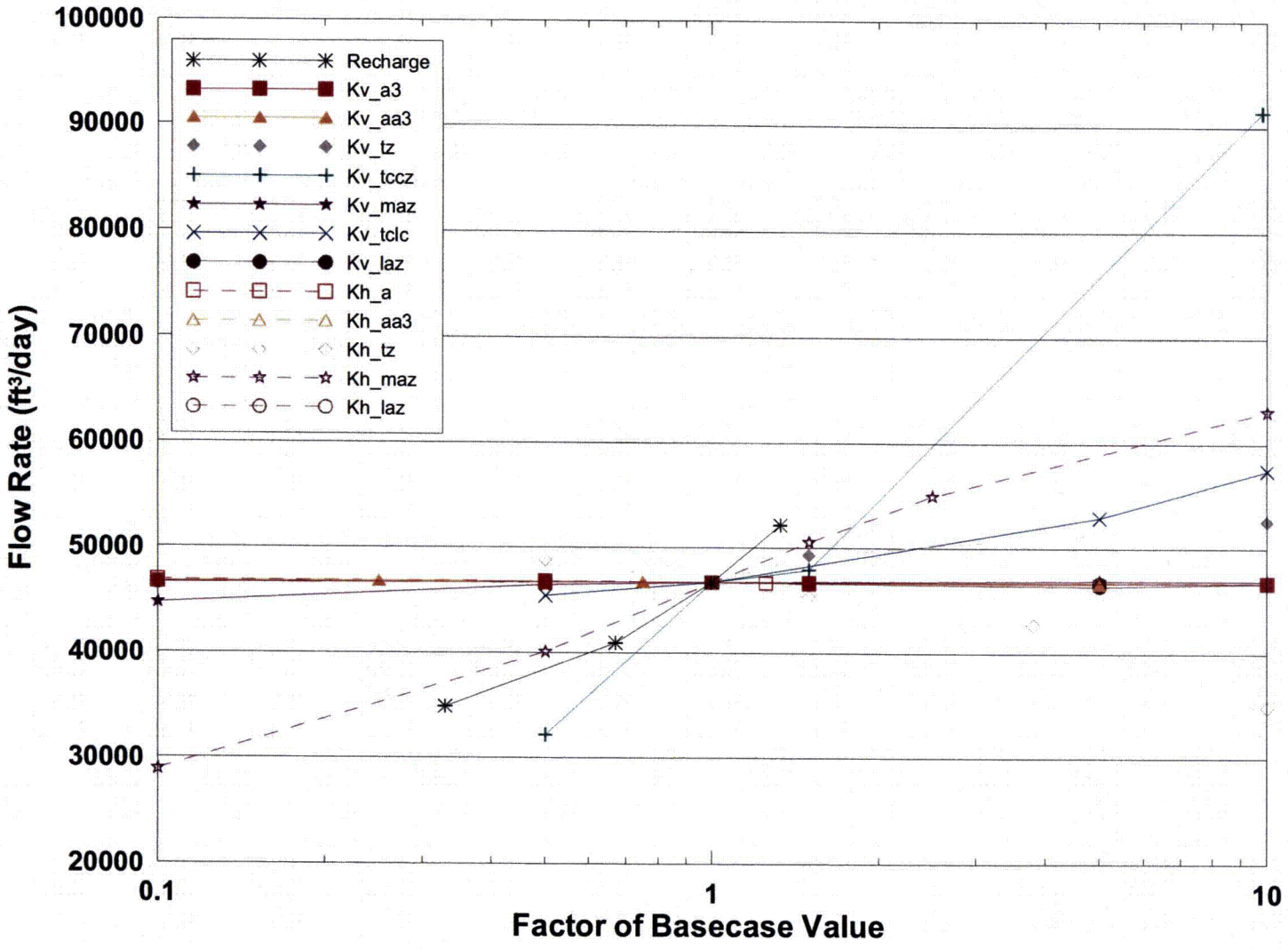

Figure 3-24. Changes in downward flow from TCCZ.

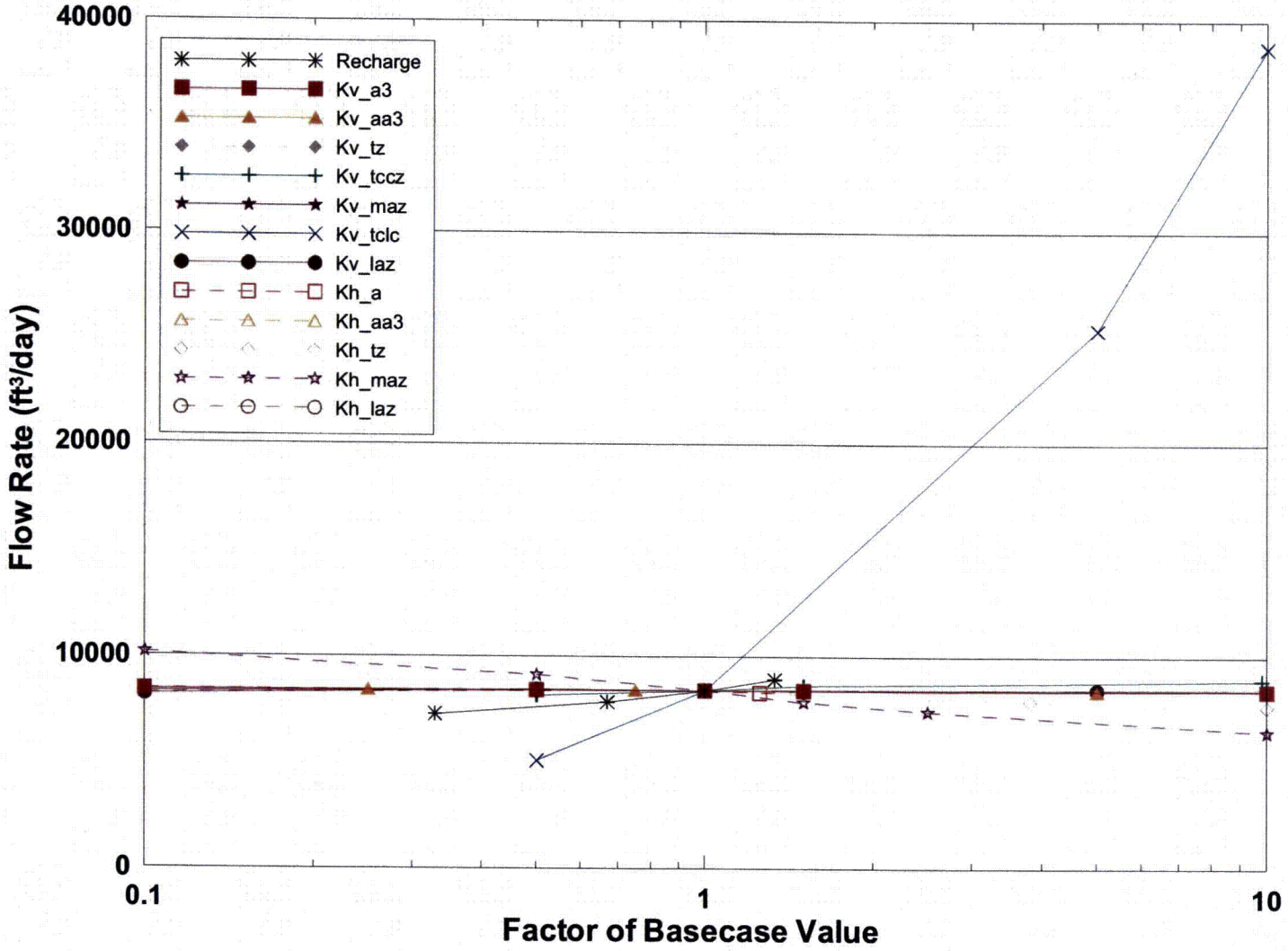

Figure 3-25. Changes in downward flow from MAZ.

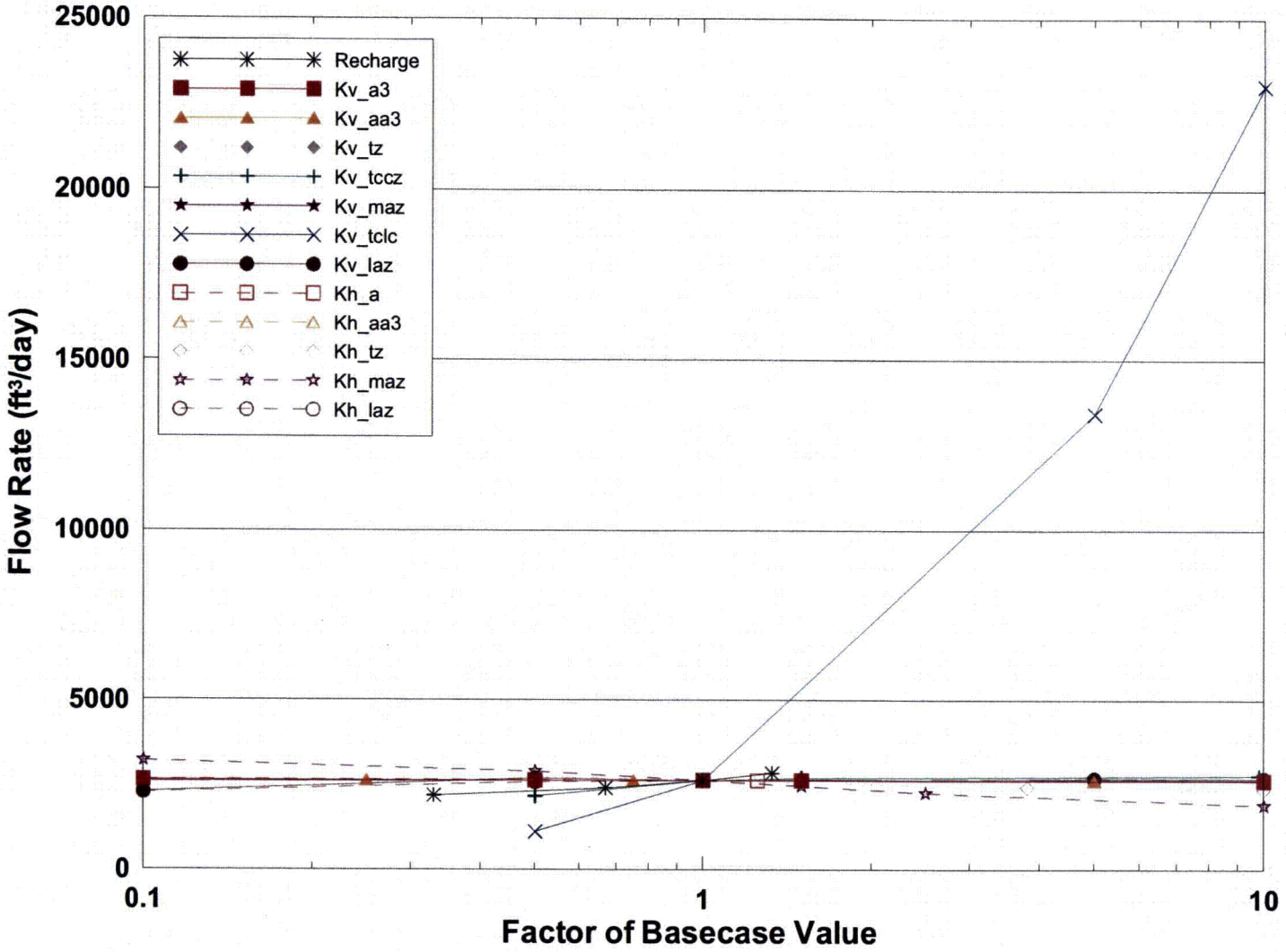

Figure 3-26. Changes in downward flow from TCLC.

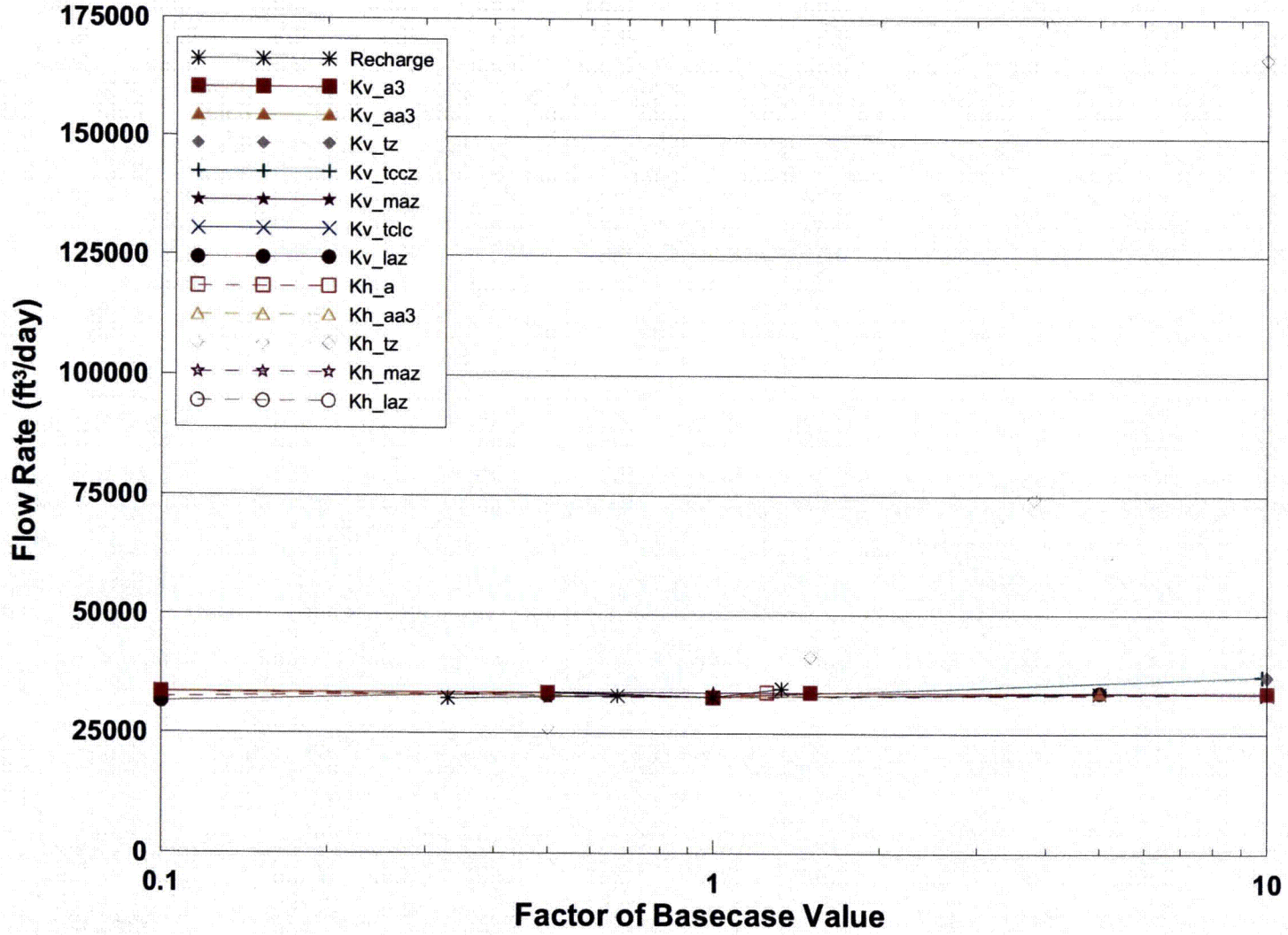

Figure 3-27. Changes in baseflows to Joyce Branch.

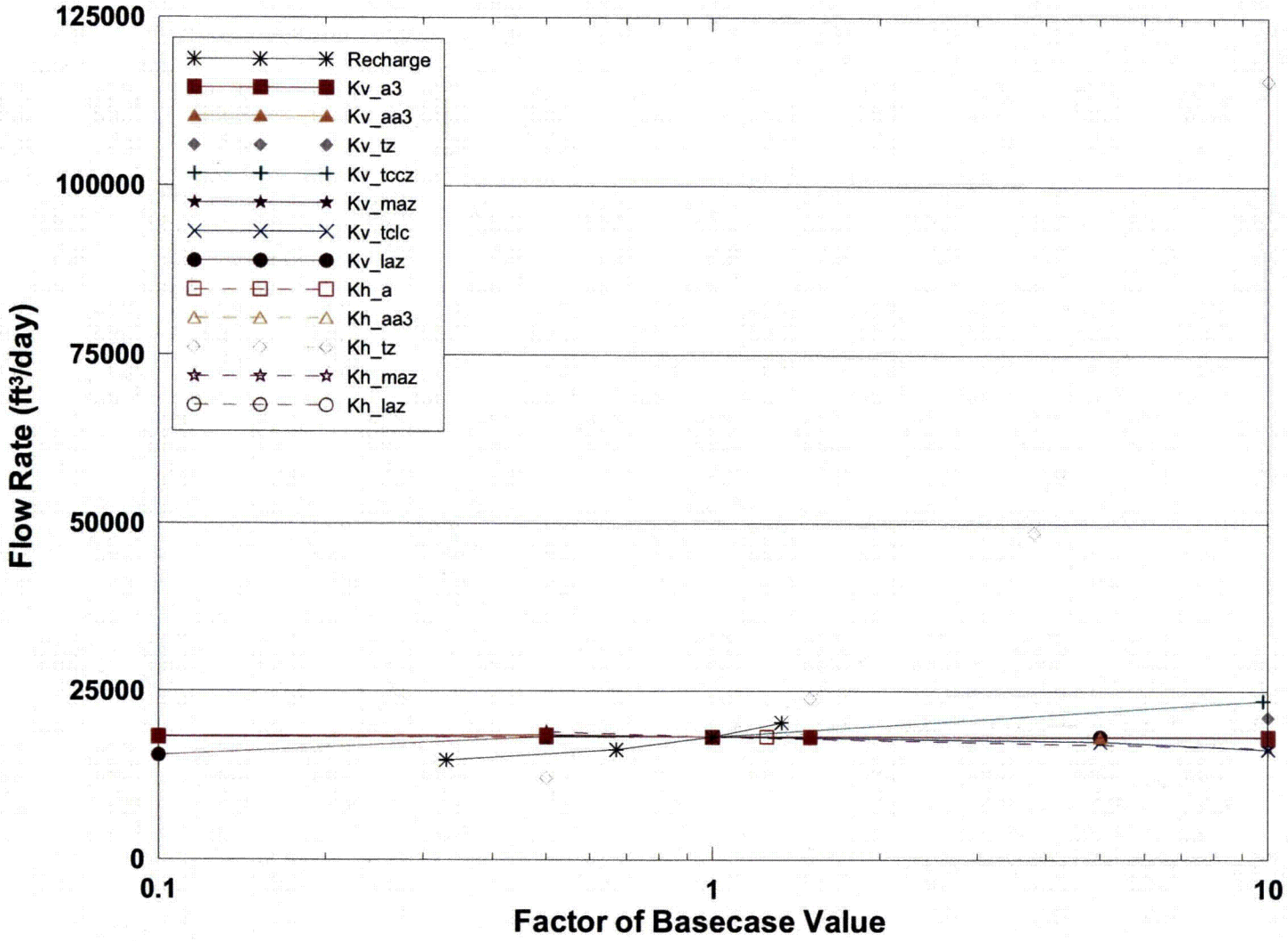

Figure 3-28. Changes in baseflows to Mill Creek.

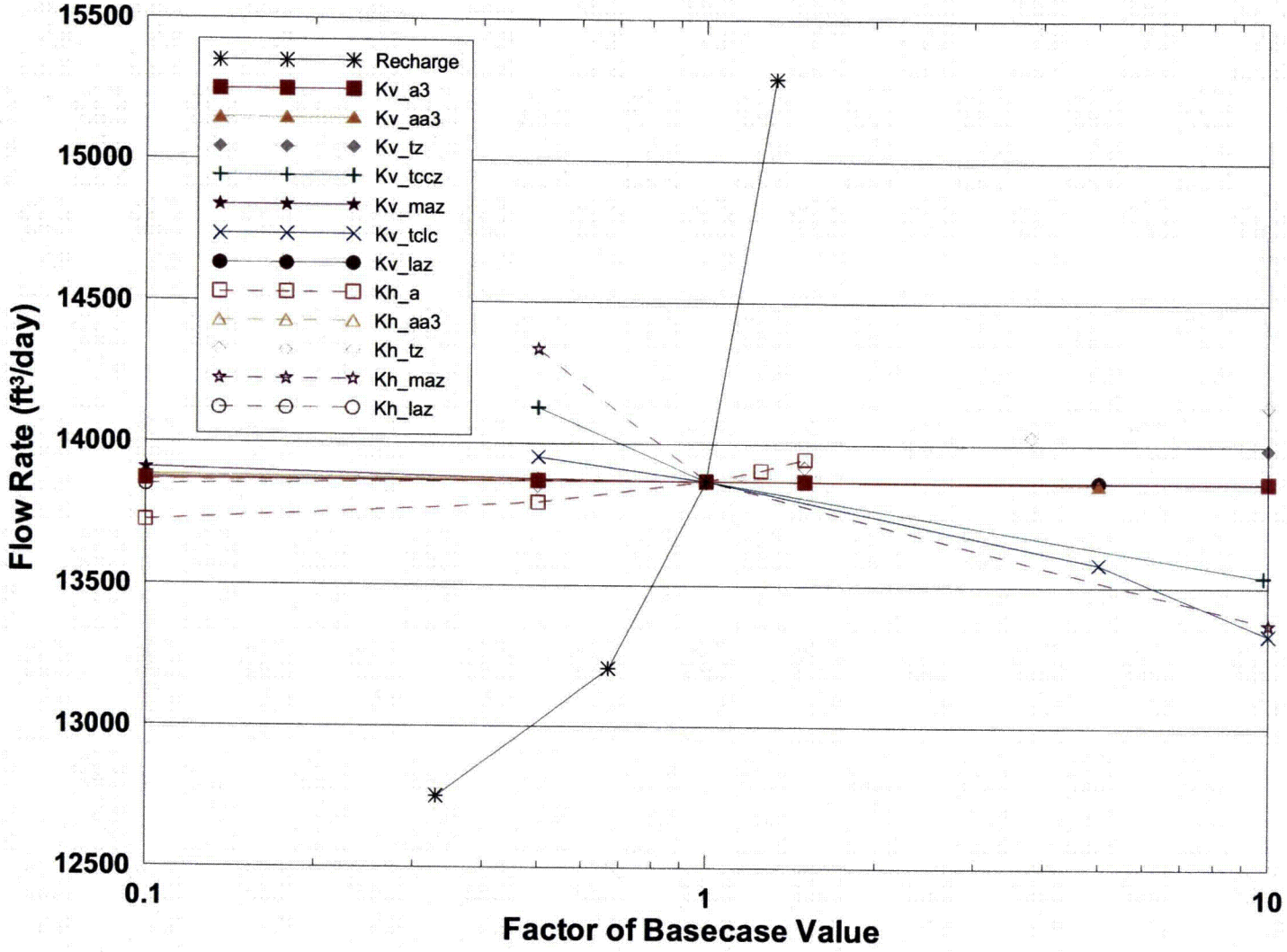

Figure 3-29. Changes in baseflows to the R-Effluent Canal and Pond A.

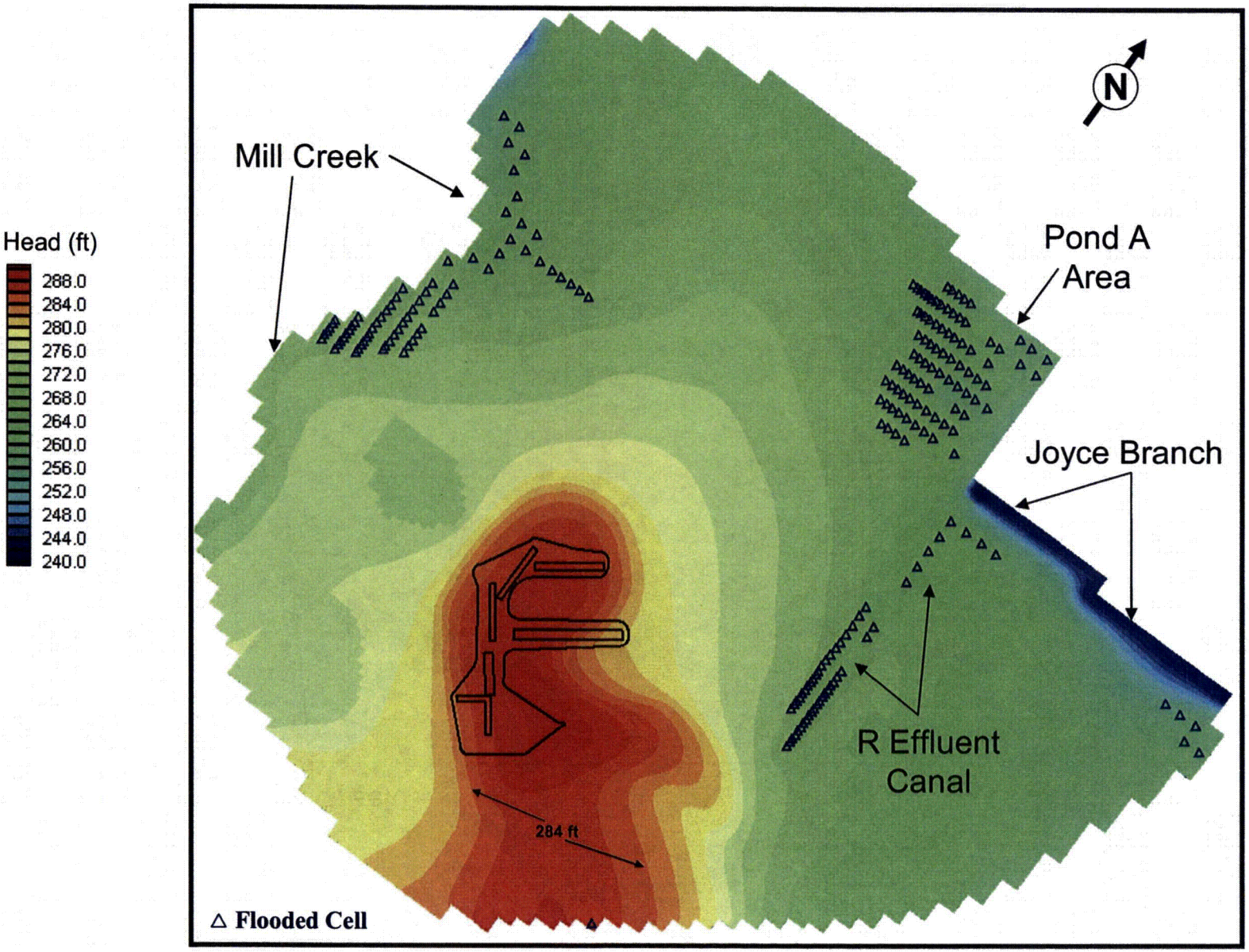

Figure 3-30. Water-table surface for the Failed Asphalt Cover flow field (recharge = 7.5 in/yr).

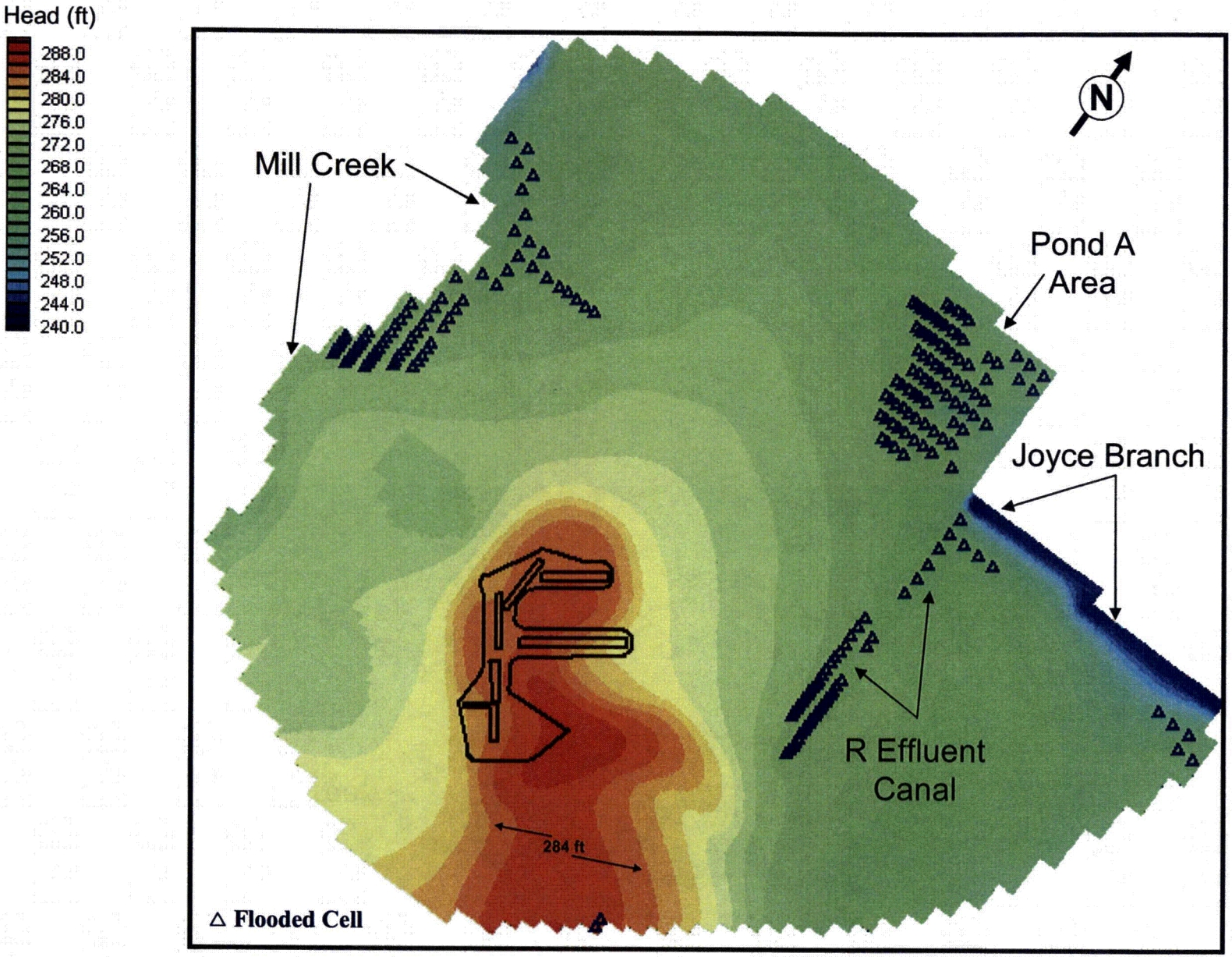

Figure 3-31. Water-table surface for the $1x10^{-5}$ cm/s Soil Cover flow field with the Existing Asphalt Cover footprint (recharge = 6.2 in/yr).

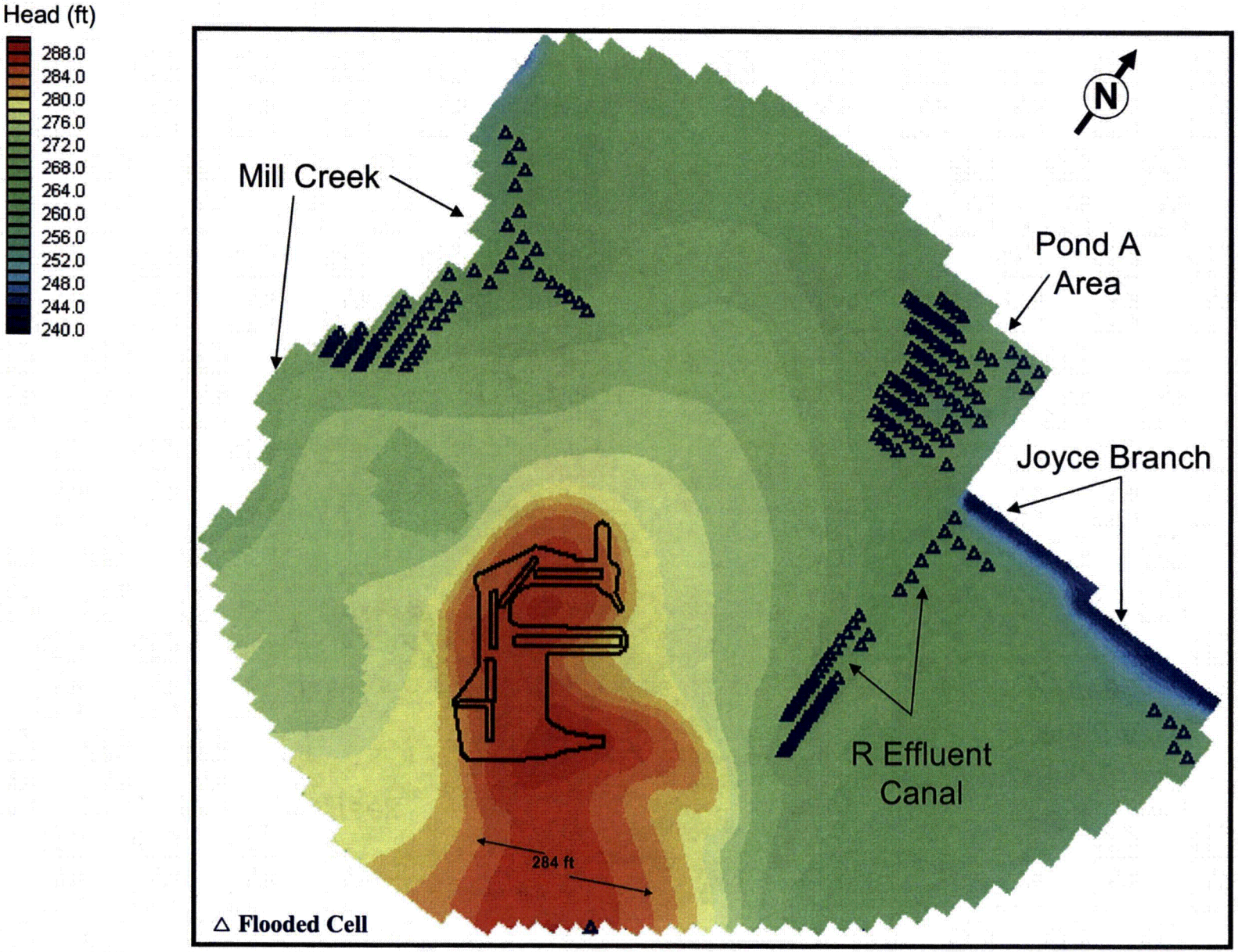

Figure 3-32. Water-table surface for the $1x10^{-5}$ cm/s Soil Cover flow field with the 15-acre cover footprint (recharge = 6.2 in/yr).

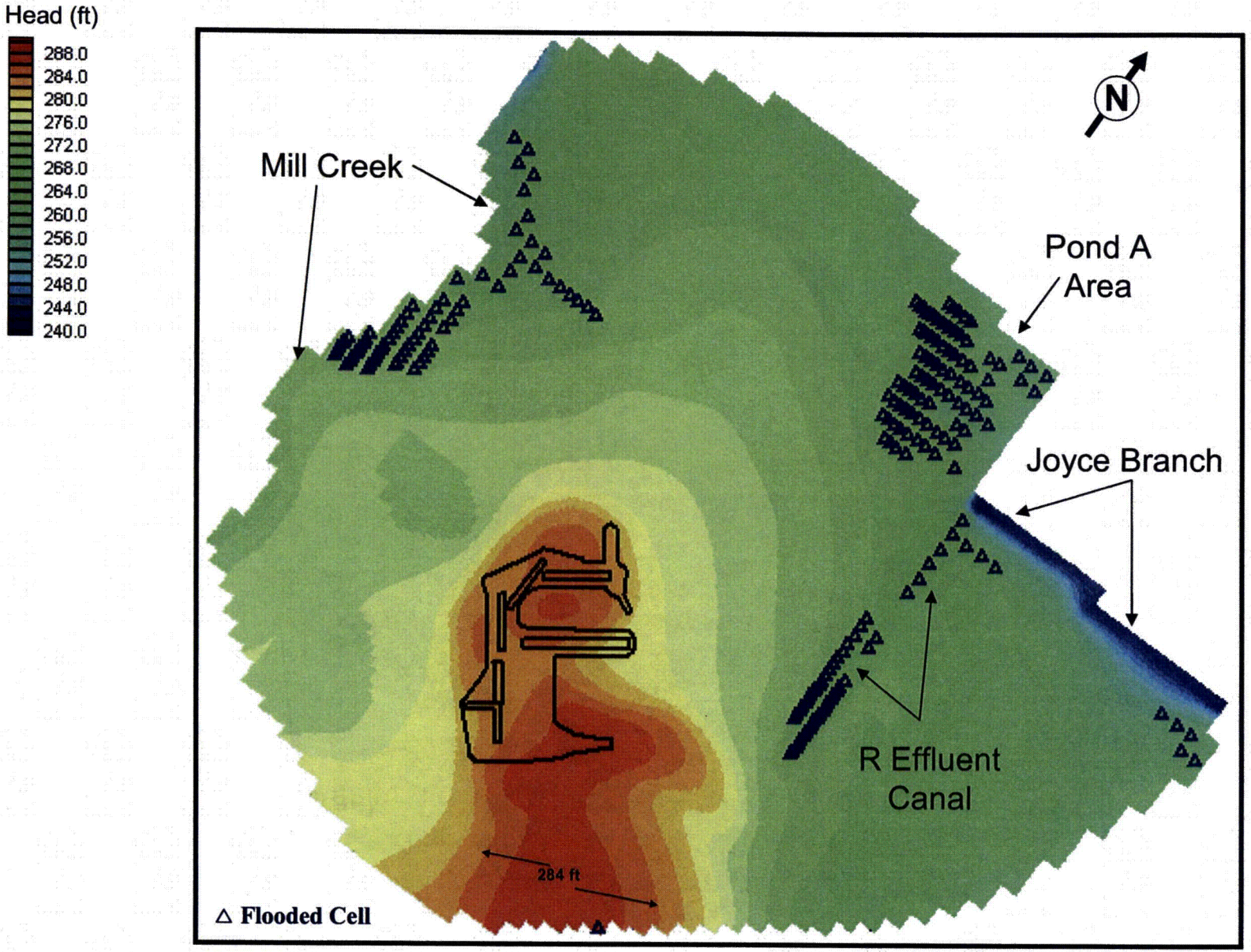

Figure 3-33. Water-table surface for the Concrete Cover flow field with the 15-acre cover footprint (recharge = 3.0 in/yr).

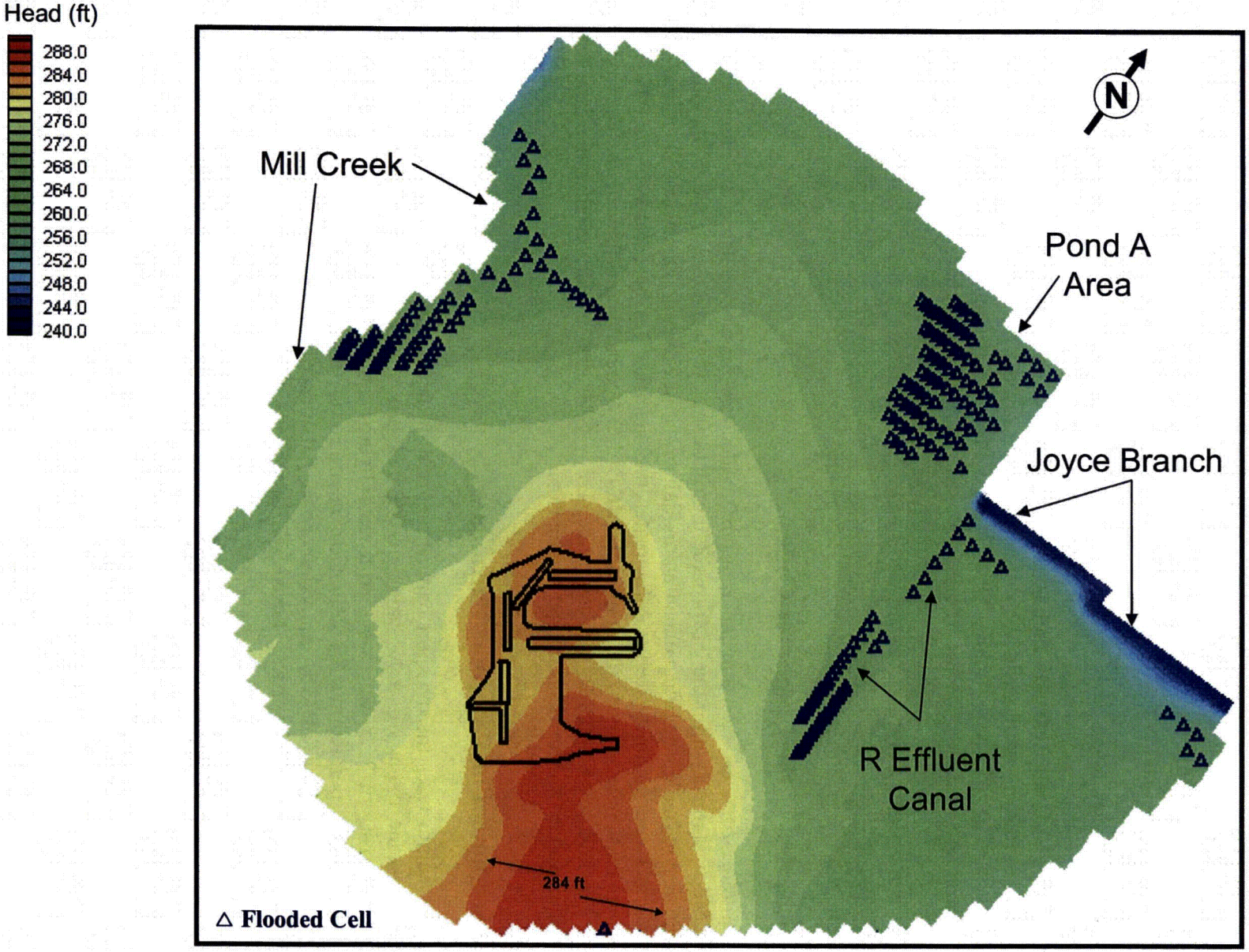

Figure 3-34. Water-table surface for the Reinforced Asphalt Cover flow field with the 15-acre cover footprint (recharge = 1.0 in/yr).

4.0 SATURATED-ZONE TRANSPORT MODEL

A series of saturated-zone contaminant transport simulations were developed to evaluate the transport of Sr^{90} within the RRSB OU shallow groundwater aquifer. The remedial alternatives were simulated to determine the feasibility of developing a GWMZ application for Sr^{90}.

As with the unsaturated-zone transport modeling, a flow model was needed to develop the saturated-zone transport model. The saturated-zone flow model was developed based on the current site conditions (existing asphalt cover). Once this model was completed, the applicable transport parameters were defined to simulate the transport of Sr^{90} for each of the remedial alternatives. The Sr^{90} concentration breakthrough curves were input directly into the saturated-zone transport simulations as the transient concentration of the recharge in specified areas. In this way, the Sr^{90} concentrations from the unsaturated-zone modeling provide the concentrations of Sr^{90} in the water infiltrating to the water table (i.e. recharge) in the saturated-zone transport modeling.

4.1 Selection of the Computer Code

The saturated-zone Sr^{90} contaminant transport model was developed using the numerical code MT3DMS contained within the GMS modeling platform. With the use of the GMS interface, a generic, or non-model specific, conceptual model can be developed. Once the conceptual model is developed and parameterized, GMS creates the specific files necessary to run MT3DMS, including creation of a link to the applicable MODFLOW steady-state flow field. The transport results generated by MT3DMS are then processed by GMS for visual presentation of the results and calculation of various mass budget summaries.

4.2 Assignment of Transport Parameters

Table 4-1 summarizes the transport parameters used in the saturated-zone modeling. As in the unsaturated-zone modeling, a K_d value of 6.0 mL/g, a bulk density of 1.69 g/cm^3, and an effective porosity of 0.25 were assigned to each hydrostratigraphic unit. Radioactive decay of Sr^{90} was also incorporated into the saturated-zone transport simulation via the use of a first-order decay term within MT3DMS, equivalent to a half-life of 28.1 years. The longitudinal, horizontal-transverse and vertical-transverse dispersivity values were set at 20, 10, and 10 ft, respectively.

Table 4-1 Summary of Transport Parameters for the Saturated-Zone Model

Parameter	Value
Bulk Density	1.69 g/cm^3
Effective Porosity	0.25
Distribution Coefficient (K_d)	6.0 mL/g
Sr^{90} Half-Life	28.1 years
Longitudinal Dispersivity	20 ft
Transverse Dispersivity (horizontal)	10 ft
Transverse Dispersivity (vertical)	10 ft

4.3 Source/Mass Loading

Studies were conducted soon after the initial release of contaminated water to the basins to estimate a total release to the environment. According to these studies, a total of 100 Ci of Sr^{90} was initially released and an estimated 78.5 Ci remained as of 1995, based on the half-life of Sr^{90} (see Table 1.1 of WSRC, 2001a). The more recent gamma-probe and soil borings resulted in a calculated activity of 53 Ci of Sr^{90} remaining in RRSB (see Table 4.9 of WSRC, 2001a). For the RRSB saturated-zone transport modeling, a total Sr^{90} activity of 89.2 Ci was assumed to be available for distribution within the unsaturated zone beneath the basins and the breached sanitary sewer line. The assumption of the 89.2 Ci is conservative and was chosen given the distribution of the source loading areas required to match the observed locations of the aqueous phase concentrations directly beneath and outside of the existing cover footprint. Therefore, the total activity available and the location of the activity within the RRSB subsurface is uncertain, but was constrained by the observed contaminated areas.

Figure 4-1 shows the model grid in the vicinity of the basins and indicates the grid cells used for source loading into the saturated zone. The unit area Sr^{90} source terms developed for Basins 1, 3, and 6 during the unsaturated-zone transport modeling were based on the activity distribution beneath the basins. These unit area source terms were converted to source terms based on model grid cell area and used to distribute the total Sr^{90} activity (89.2 Ci) among the six basins and to areas outside of the basin footprints (see Figure 4-1). Because no source term information was available for Basins 2, 4, and 5, the source terms for Basins 1 and 6 were used to load these basins. For example, the Sr^{90} source term developed for Basin 1 was used as the source term for Basins 1 and 2, and the areas to the south and east of Basin 1 which are located under the cover footprint. For the areas outside of the cover footprint, the Sr^{90} source term for Basin 1 under ambient recharge conditions (15 in/yr) was assigned. Similarly, the Basin 6 source term was used for Basins 4, 5, and 6. The source loading in Figure 4-1 shows that a majority of the activity is assumed to be located in the unsaturated zone below the Basin 1 source loading cells.

To couple the results of the unsaturated-zone transport modeling to the saturated-zone transport modeling, the transient Sr^{90} concentration curves developed during the unsaturated-zone transport modeling were then loaded into the corresponding saturated-zone transport model grid cells as the transient Sr^{90} concentration in the recharge entering the water-table surface. The raw output from the unsaturated-zone models yielded aqueous concentrations in mg/L. These concentrations were converted to ng/L prior to importing into the saturated-zone models. The conversion from mg/L to ng/L was conducted to minimize the potential for any numerical effects (i.e. rounding or dispersion) on the simulation results given the expected low simulated concentrations values. The time-stepping of the MT3DMS saturated-zone transport model was designed such that the detailed transient nature of the concentration to the water table could be accurately incorporated into the saturated zone through the simulation time of 400 years.

In the initial configuration of the transport model, the initial concentrations within the "A" and the "AA" were assumed to be zero. This assumption was made to determine if the observed concentrations outside of the basin footprints to the south and east of Basin 1 were a result of contamination from the basins proper or from the breached sanitary sewer line. During this initial simulation, it was determined that the transport direction from the RRSB, which is predominantly vertical, could not explain the observed contamination to the south and east.

Therefore, the source loading of mass outside of the basin footprint is required to account for the concentrations observed to the south and east.

The saturated-zone transport simulations assumed a starting time of 1998 with the source term distributed as discussed above. The historical mass loading to the water table prior to 1998 was not simulated. Therefore, to account for the observed Sr^{90} mass within the saturated zone, WSRC developed a map of initial concentrations within the "A" and "AA" horizons (Figure 4-2), based on the 1995 through 2001 observed Sr^{90} soil and groundwater concentrations. This map was used to define the initial Sr^{90} concentrations in the groundwater for the saturated-zone transport simulations.

4.3 Assumptions

The development of the saturated-zone transport model was based on a set of assumption which were necessary given the limitations in the understanding of the site conditions. These assumptions are:

- a single K_d value was used for all hydrostratigraphic units;
- a total of 89.2 Ci of Sr^{90} is adsorbed to the soils beneath the RRSB;
- the spatial distribution of the Sr^{90} within the model reflects the actual distribution;
- the Sr^{90} activity distribution for Basin 1 is applicable as the source term for Basin 2 and the areas located outside of the basins;
- the Sr^{90} activity distribution for Basin 6 is applicable as the source term for Basins 4 and 5; and
- the initial Sr^{90} groundwater concentration map developed from the observed soil and groundwater data correctly reflects the existing groundwater concentrations.

4.5 Results

Figure 4-3 presents a plan view of the RRSB area and indicates the location of cross-sectional lines that will be used to present and discuss the results of the saturated-zone transport simulations. The cross-sectional lines were placed such that two views through the high-concentration areas to the south and east of Basin 1 (A-A' and C-C') could be obtained and also a view through the northern edge of Basin 3 (B-B') which is the northernmost location of the initial Sr^{90} concentrations within the aquifer. Three TZ observation points were selected in an area where simulated concentrations greater than the MCL were observed. These observation points were used to develop time series plots of Sr^{90} concentrations in the TZ for all of the remedial alternatives simulated in this study. The simulated concentrations output from the saturated-zone model were in units of ng/L. These concentrations were then converted to pCi/L,

using the specific activity value contained in Table 2-1, prior to development of the cross sections and time series plots.

Figure 4-4 shows the time series plot for the Existing Asphalt Cover simulation at the TZ observation points. The locations of the observation points are shown in the insert to Figure 4-4. Figure 4-5 presents plan-views of Sr^{90} concentrations above the 8 pCi/L MCL within the "A" horizon of the model at simulation times of 20, 50, 100, 200, 300, and 400 years. This figure shows that with the current asphalt cover, minimal lateral migration of Sr^{90} occurs during the 400 year simulation period. This lack of lateral migration is a result of the strong vertical gradients within the portions of the "A" horizon, "AA" horizon, and TZ located beneath the RRSB. The maximum Sr^{90} concentrations in the "A" horizon are reached between 20 and 50 years and decline after 100 years. By 300 years, concentrations above the MCL are not present within the "A" horizon, except beneath the source loading area located outside the cover footprint to the south and east of the asphalt cover.

Cross-sectional views, along the lines of section depicted in Figure 4-3, are shown in Figures 4-6 through 4-8. These figures show that vertical migration dominates the transport of Sr^{90} during the simulation period. The maximum vertical extent of Sr^{90} concentrations above the MCL reaches the TCCZ within 50 years. As in the plan view figures, the maximum concentrations appear to peak between 20 and 50 years, and decline after 100 years. This observation is supported by the time series plot for Sr^{90} concentrations (Figure 4-4). Figure 4-9 presents plan views of the Sr^{90} concentration in the upper model layer within the TZ at simulation times of 10 years and 145 years, along with the location of the observation points. These plots represent the maximum lateral extent of Sr^{90} at early time (10 years) as a result of the downward migration of the initial concentrations and the subsequent maximum lateral extent at later times (145 years) as a result of the transient recharge concentration source terms. These results show that the distribution coefficient (K_d = 6.0 mL/g) and subsequent retardation value (R = 41) for Sr^{90} yield very limited transport distances over relatively long simulation times. The results also show that the lack of observable concentrations within the RRSB groundwater at locations other than in the immediate vicinity of the basins or in the location of the breached sanitary sewer line are a result of the vertical transport pathways within the UAZ.

4.6 Transport Model Sensitivity Analysis

A sensitivity analysis was performed for the Existing Asphalt Cover transport simulation in order to determine which parameters may cause the largest amount of uncertainty in the transport results. Additionally, the sensitivity analysis provides a better understanding of the important parameters in the transport of Sr^{90} within the R-Area and information about which parameters may need to be more specifically quantified for future modeling of the site. The parameters varied for the sensitivity test cases were longitudinal dispersivity, porosity, and K_d. The steady-state flow field for the Existing Asphalt Cover, as described in Section 3.0, was used as the starting point for each of the transport sensitivity test cases and source loading was not varied for any of the test cases. Curves of the transient Sr^{90} concentration, measured at the same locations within the TZ as presented in Figure 4-4, are presented in Figures 4-10a through 4-10d for each sensitivity test case. Figures 4-10a through 4-10c present the transient concentration curves at

the three observation locations, respectively, for all of the sensitivity simulation results, except for the results of a simulation with a K_d = 0.6 mg/L, which are presented in Figure 4-10d.

4.6.1 Longitudinal Dispersivity

For longitudinal dispersivity, values of 10 ft and 40 ft were selected for simulation, compared to the basecase value of 20 ft. Since horizontal and vertical transverse dispersivity were modeled within the basecase simulation as a fraction of the basecase longitudinal dispersivity, 0.5, this was also used in the sensitivity test cases. The curves for the longitudinal dispersivity equal to 10 ft (Figure 4-10) show lower peak concentrations within the TZ when compared to the basecase simulation. Similarly, the times to peak concentration are slightly retarded when compared to the basecase. Figures 4-11 through 4-13 show the cross sections, for the lines of section depicted in Figure 4-3, for the test case performed with a longitudinal dispersivity of 10 ft. When compared to the basecase results, there is a slight decrease in the vertical transport distances for both the contaminated areas located under and outside the asphalt cover.

For the transient concentration curves based on a longitudinal dispersivity equal to 40 ft (Figure 4-10), the peak Sr^{90} concentrations are higher than the basecase peaks and occur at slightly earlier times. Figures 4-14 through 4-16 show the cross sections for the test case performed with a longitudinal dispersivity of 40 ft. These cross-sectional views show that there is an increase in the vertical transport distance, especially within the region of the Basin 1 source loading areas.

4.6.2 Distribution Coefficient (K_d)

For the K_d test cases, values of 0.6 mL/g and 60 mL/g were selected, compared to the basecase value of 6 mL/g. The curves for K_d equal to 0.6 mL/g (Figure 4-10d) show significantly higher peak concentrations as compared to the basecase simulation. Cross-sectional views for this test case (Figures 4-17 through 4-19) also show quick vertical transport of Sr^{90} through the upper hydrostratigraphic units, with significant lateral transport in the TZ, MAZ, and LAZ. Concentrations above the 8 pCi/L MCL reach the LAZ within 50 years and subsequently decrease to below the MCL between 200 and 300 years.

The transient concentration curves for a K_d value of 60 mL/g are presented in Figure 4-10. These curves and the cross-sectional views for this test case (Figures 4-20 through 4-22) show less vertical migration of Sr^{90} as a result of the higher sorption coefficient and retardation. No concentrations above the 8 pCi/L MCL were simulated at observation points #1 and #3. The transient concentration curve for observation point # 2 does show concentrations above the MCL, which is a result of vertical transport of the initial concentrations assigned in the overlying "AA" horizon.

The significant differences in the results of the K_d sensitivity analyses suggest that specific K_d values for each hydrostratigraphic unit would have a large impact on the distribution of Sr^{90} within the saturated zone.